

Phase-Field Modeling of Fracture for Ferromagnetic Materials through Maxwell's Equation

Nima Noii^{a,b,1}, Mehran Ghasabeh^c, Peter Wriggers^{b,d}

^a Deutsches Institut für Kautschuktechnologie (DIK e.V.)
Eupener Straße 33, 30519 Hannover, Germany

^b Institute of Continuum Mechanics
Leibniz Universität Hannover, An der Universität 1, 30823 Garbsen, Germany

^c Chair of Soil Mechanics and Foundation Engineering
Technische Universität Bergakademie Freiberg, 09599 Freiberg, Germany

^d Cluster of Excellence PhoenixD (Photonics, Optics, and Engineering - Innovation Across Disciplines), Leibniz Universität Hannover, Germany

Accepted in Engineering Fracture Mechanics

ISSN 00137-944

Abstract

Electro-active materials are classified as *electrostrictive* and *piezoelectric* materials. They deform under the action of an external electric field. *Piezoelectric* material, as a special class of active materials, can produce an internal electric field when subjected to mechanical stress or strain. In return, there is the converse piezoelectric response, which expresses the induction of the mechanical deformation in the material when it is subjected to the application of the electric field. This work presents a variational-based computational modeling approach for failure prediction of ferromagnetic materials. In order to solve this problem, a coupling between magnetostriction and mechanics is modeled, then the fracture mechanism in ferromagnetic materials is investigated. Furthermore, the failure mechanics of ferromagnetic materials under the magnetostrictive effects is studied based on a variational phase-field model of fracture. Phase-field fracture is numerically challenging since the energy functional may admit several local minima, imposing the global irreversibility of the fracture field and dependency of regularization parameters related discretization size. Here, the failure behavior of a magnetoelastic solid body is formulated based on the Helmholtz free energy function, in which the strain tensor, the magnetic induction vector, and the crack phase-field are introduced as state variables. This coupled formulation leads to a continuity equation for the magnetic vector potential through well-known Maxwell's equations. Hence, the energetic crack driving force is governed by the coupled magneto-mechanical effects under the magneto-static state. Several numerical results substantiate our developments.

Keywords: Maxwell's equation, phase-field fracture, magnetization, magnetostriction, Ferromagnetic, magnetic vector potential, electric field, magnetic field, magnetomechanical.

¹Corresponding author (Nima Noii).

Contents

1. Introduction	2
2. Phase-field modeling of fracture for ferromagnetic materials	6
2.1. Primary fields for the multi-field problem	6
2.2. Governing equations of the failure mechanism for magnetostrictive effects .	9
2.2.1. Elastic contribution	9
2.2.2. Electromagnetic contribution	10
2.2.3. Fracture contribution	15
2.2.4. Transition structure from undamaged to fully damaged states . . .	17
3. Energy quantities and variational principles	19
3.1. Constitutive functions	19
3.1.1. Energy quantities	19
3.1.2. Magnetization contribution	20
3.1.3. Magnetostrictive contribution	20
3.1.4. Elastic contribution	21
3.1.5. Fracture contribution	24
3.2. Variational formulations for the coupled multi-field problem	24
3.2.1. Electromagnetic contribution	25
3.2.2. Elastic contribution	25
3.2.3. Fracture contribution	25
3.3. Space finite element discretization	28
4. Numerical examples	29
4.1. Example 1: Magnetostatic problem for transient magnetic vector potential	29
4.2. Example 2: Magneto-mechanically induced cracking in an iron beam sur-	
rounded by vacuum	31
4.3. Example 3: Magneto-mechanically induced cracking in a ferromagnetic	
material containing predefined notches and wires	33
4.3.1. Sub-example 1: Transversely wired plate with three winding wires .	33
4.3.2. Sub-example 2: Transversely wired plate with nine winding wires .	33
4.3.3. Sub-example 3: Longitudinally wired plate with four winding wires	34
4.3.4. Sub-example 4: Longitudinally wired plate with five winding wires .	35
5. Conclusion	43
References	46

1. Introduction

Active materials are a particular type of material that undergoes mechanical deformation in response to external effects. The sources of these effects can be pressure, thermal, electric, and magnetic fields [1]. In the literature, these materials are known as smart materials. There are various types of active materials, such as shape memory alloys, electrostrictive elastomers, piezoelectric materials, ferroelectric materials, and electro- and magneto-active polymers. [2, 3]. The basic mechanical properties of active materials, such as strain generation capability, stiffness, strain, Hysteresis and electrical impedance

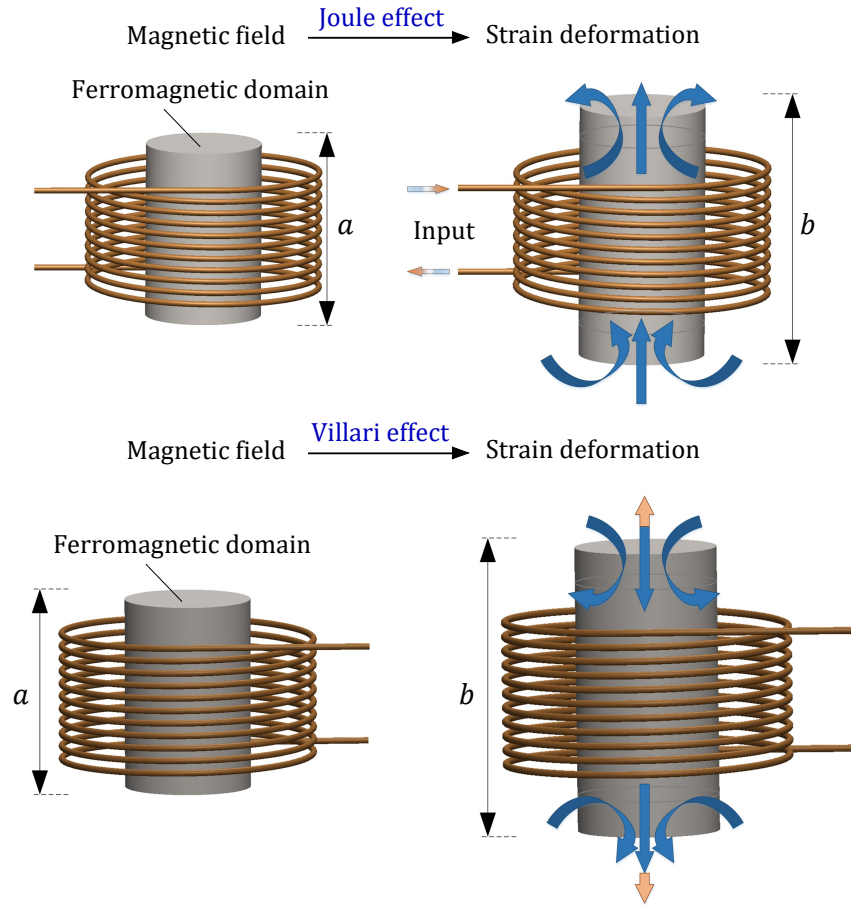


Figure 1: Schematic representation of Joule effect (direct magnetostrictive effect) in the first row and Villari effect (reversible magnetostrictive effect) in the second row.

vary widely. The energy output of active materials used in actuators is principally dominated by stiffness and the amount of strain energy generated by the material [1]. The materials can be classified according to their response when they are subjected to external stimuli. To this end, active materials can be generally categorized as electro-active and magneto-active materials.

Electro-active materials are classified as *electrostrictive*, and *piezoelectric materials*. These materials deform mechanically under an external electric field. Piezoelectric materials can produce an internal electric field when subjected to mechanical stress or strain (direct piezoelectricity) [4]. Piezoelectric materials also represent the reverse piezoelectric effect (converse piezoelectricity), where stress or strain is generated when they are subjected to an electric field [5]. The direct piezoelectric response of material is determined by the conversion of the mechanical into the electrical energy; however, the converse piezoelectric response expresses the induction of mechanical deformation as a consequence of the applied electric field [6]. Piezoelectric materials are applied within a great range, including piezoelectric motors, actuators in industrial sector, sensors in the medical sector, actuators in consumer electronics (printer, speakers), piezoelectric buzzers, piezoelectric igniters, microphones, nanopositioning in atomic force microscope (AFM) and the scanning tunneling microscope (STM), and micro-robotics (defense) [7].

Electrostrictive materials generate stress or strain when subjected to an external elec-

tric field [1]. However, there is a principal difference between piezoelectric and electrostrictive materials. The piezoelectric effect is possible only in non-centrosymmetric materials. However, the electrostrictive effect is not limited by symmetry and is present in all materials, even those that are amorphous. Therefore, the electrostrictive effect exhibits a nonlinear (second-order or quadratic) dependency of the strain on the applied electric field [6].

Magnetostriction, a key feature of magnetic materials, is defined as the alteration in shape and dimension of the material during the magnetization process. It continues till the magnetic saturation of the material is attained. The magnetostriction phenomenon was first introduced in the work of Joule [8]. It is also known as the Joule effect. In 1846, Villari discovered the reverse effect of magnetization (see Figure 1)[9]. Ferromagnetic material and ferri-magnetic are known for their magnetostrictive characteristics. A magnetostrictive material consists of tiny fragments. These fragments, usually iron, nickel, or cobalt, have small magnetic moments as a result of their "3d" shells that are not completely filled with electrons. Ferromagnetics fundamentally acts like tiny permanent bar magnets. Magnetic materials have a property of magnetostriction that causes them to change their shape or dimensions during the magnetization process. Such materials can convert magnetic energy into kinetic or reverse and thus are mainly used to construct actuators and sensors. The applicability of the materials is quantified by the magnetostrictive coefficient. It is defined as the fractional change in length as the magnetization of the material increases from zero to the saturation value. This coefficient can be positive and negative. The magnetostriction characteristic induces energy loss due to frictional heating in susceptible ferromagnetic cores. It also produces the low-pitched humming sound that can be heard coming from transformers, where an existing magnetic field is changed by oscillating AC currents.

In the literature, computational approaches to modeling the electromagnetic response of the electro- and magneto-active materials are developed within a framework of thermodynamics. For some active-material, it is sufficient to take into account only a quasi-static state for modeling the magnetic response [10]. The work proposes a hybrid SBFEM-FEM approach for efficiently calculating stray magnetic fields in unbounded domains. Most of the works aim at constructing a coupling between electromagnetics and mechanics. The key feature of these approaches is to investigate the stress response of the materials under the electro- and magneto-striction effects. The coupled formulation within the framework of magnetoelasticity is found in the work of Brigadnov and Dorfmann [11] where a mathematical model is developed to investigate the mechanical characteristics of the magneto-sensitive elastomer under the application of a magnetic field. Further studies related to magneto-sensitive elastomers are conducted in the work of Dorfmann, and his colleagues [12, 13]. The investigation of an electromagnetic forming process is conducted in [14] by formulating a fully coupled electromagnetic-thermomechanical model. A computational approach incorporating the energy-based magneto-mechanical model is developed in [15, 16, 17] for the electric electrical steel sheets. An energy-density functional method is proposed in [18] based on an isotropic spline-based thermodynamic approach to model magneto-mechanical behavior in ferromagnetic material.

Electro-magneto-mechanical coupling effects are formulated, based on incremental variational principles, within a general continuum mechanics framework and numerical implementation of dissipative functional materials in [19]. Micromagnetics is another

concept where a geometrically consistent incremental variational formulation is extended in a micro-magneto-elastic model that accounts for the micro-structural evolution of both magnetically- and mechanically-driven magnetic domains in ferromagnetic materials [20]. The variational-based computational modeling of ferromagnetics and magnetorheological elastomers, which present a mutually-coupled magneto-mechanical response, is proposed in [21]. Further study on the behavior of magnetosensitive polymers based on a multiplicative magneto-elastic model within a micromechanically-based framework is found in [22]. Moreover, models regarding the thermomechanical effects are developed to investigate the coupling between electromagnetics and thermomechanics in [23] for electric motors. The multi-physics problem regarding magnetic-thermal-mechanical modeling of the electromagnetic rail launching is investigated in [24]. The principles of designing an in situ fatigue testing system, including structural resonances, transient response, grip design, and thermal insulation performance of the device, are studied in detail in [25] by developing a coupled thermo-mechanical model. The Cell-based smoothed finite element method (CS-FEM) and the asymptotic homogenization method (AHM) is incorporated in [26] to simulate the magneto-electro-elastic response of a structure under dynamic load accurately.

In engineering applications, predicting crack initiation and propagation in structures under mechanical loading and environmental conditions is greatly important. Besides classical approaches for fracture mechanics, non-local damage models and variational approaches have been developed in the literature. The non-local damage models have been formulated to overcome the ill-posedness due to spatial discretization in finite element simulations. The variational approaches are introduced based on energy minimization [27, 28, 29], and their regularization is obtained by Γ -convergence, which is fundamentally inspired by the work of image segmentation conducted by Mumford and Shah [30]. The model is then improved by formulating a Ginzburg-Landau-type evolution equation of the fracture phase-field [31]. In recent years, the variationally-based phase-field approach to fracture within the thermodynamically consistent framework is proposed in the work of Miehe et al. [32]. In the latest work, the robust algorithmic formulation of the evolution of diffuse crack topology in time is proposed by introducing a local history field that determines the maximum tensile strain obtained in history. It then acts as a crack driving force in the evolution of the crack phase field. In the literature, few works investigate the material's cracking response; for example, in [33], the failure mechanism of piezoelectric is studied by extending electromechanics to the phase-field approach. Ferroelastic ceramics is another class of active material in which the crack initiation and propagation are examined in [34], which proposes a computational framework that regards the electric displacement saturation and its effect on the hysteretic behavior of ferroelectric ceramics and the resulting cracking response.

This work applies the phase-field approach to the magneto-mechanically driven fracture in ferromagnetic materials. In the formulations for examining the response of the electromagnetic materials, finite element method (FEM) is applied to discretize the time-dependent Maxwell's equations on a bounded domain in three-dimensional space. At first, the formulation is developed by deriving a weak formulation for the electric and magnetic fields with approximate Neumann and Dirichlet boundary conditions, and the problem is discretized both in time and space. In general, the electric and the magnetic fields are discretized by adapting *Nédélec* curl-conforming and *Raviart-Thomas* div-conforming finite element approaches, respectively.

The main objective of this contribution is to introduce:

- Extension of Maxwell's equations towards a coupled magneto-mechanical model to investigate the stress response of the ferromagnetic materials;
- Transition rule for the electromagnetic material properties from undamaged to fully damaged states through the fracture phase-field, which acts as a geometric interpolation variable;
- Investigation of the magnetostrictive-induced cracking in the ferromagnetic materials by developing a magneto-mechanical model coupled with the phase-field model;
- Representation of numerical examples to substantiate our developments in predicting the fracture response of the ferromagnetic material.

The paper is structured as follows: For a better insight into phase-field modeling of fracture for ferromagnetic materials, primary fields for the multi-field problem are provided in Section 2. Through a regularized fracture phase-field formulation, we further outline the theoretical framework for magnetostrictive-induced fracture in ferromagnetic materials. The transition rule for the electromagnetic material properties from undamaged to fully damaged states is also discussed. Next, Section 3 outlines the constitutive energy density for the magneto-mechanical formulation of fracturing solids, which suffices to define the variational formulation setting. In Section 4, three numerical simulations are performed to demonstrate the correctness of our algorithmic developments. Finally, the paper is concluded with some remarks.

2. Phase-field modeling of fracture for ferromagnetic materials

This section outlines a mathematical model for magnetostrictive-induced cracking in ferromagnetic materials by developing a magneto-mechanical model, considering small deformations. The fracture process is modeled by employing the well-developed phase-field formulation to resolve the sharp crack surface topology in the regularized concept. We specifically elaborate *three governing equations* to characterize the constitutive formulations for the mechanical deformation, electromagnetic as well as the fracture phase-field. This coupled formulation is derived by obtaining a continuity equation for the magnetic vector potential through well-known *Maxwell's equations*. Thus, the comprehensive objective of the following section is to advance a continuum theory of cracking response in ferromagnetic materials within a framework of thermodynamics.

2.1. Primary fields for the multi-field problem

Let $\Omega \subset \mathbb{R}^\delta$ be an arbitrary vacuum free space box with dimension $\delta = \{2, 3\}$ and $\mathcal{B} \subset \mathbb{R}^\delta$ denote the domain occupied by the material solid, as demonstrated in Figure 2. Vacuum space Ω is considered to be large enough such that the magnetic field induced by the magnetization of the body \mathcal{B} is decayed at its surface $\partial\mathcal{B} \subset \mathbb{R}^\delta$. Also, in the following, let a Dirichlet boundaries conditions of vacuum defined as $\partial_D\Omega = \partial_D^0\Omega \cup \partial_D^1\Omega$ which contains inner surface (it has an intersect with the solid body \mathcal{B}) and outer boundary surface, respectively, as shown in Figure 2b . We further assume Dirichlet boundary conditions on $\partial_D\mathcal{B}$ and complete Neumann boundary conditions on $\Gamma_N := \partial_N\mathcal{B} \cup \mathcal{C}$, where

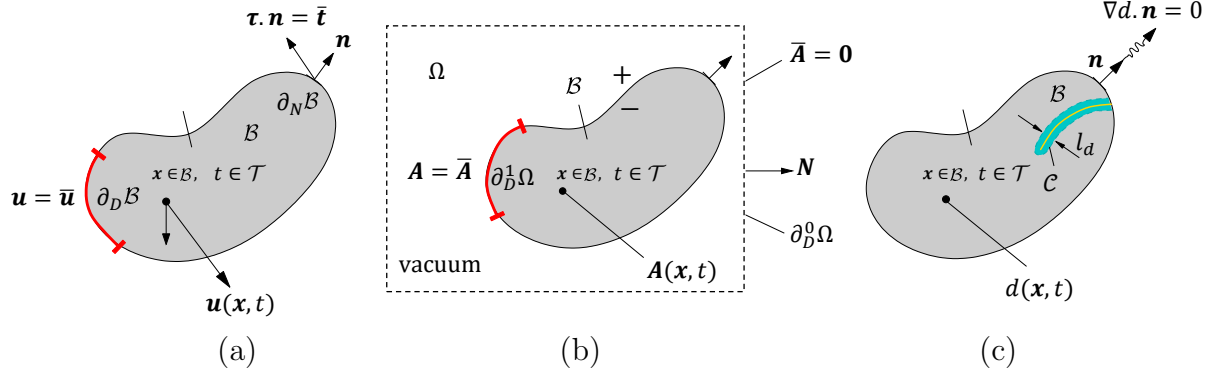


Figure 2: Primary variable fields in magneto-elasticity, for a solid body $\mathcal{B} \subset \mathcal{R}^\delta$ with dimension $\delta \in [2, 3]$. (a) The displacement field \mathbf{u} defined on \mathcal{B} and Neumann-type boundary condition for traction $\bar{\mathbf{t}} = \boldsymbol{\tau} \cdot \mathbf{n}$ on $\partial_N \mathcal{B}$. (b) The magnetic vector potential \mathbf{A} in Ω that is continuous across the interface $\partial \mathcal{B}$, i.e. $\llbracket \mathbf{A} \rrbracket := \mathbf{A}^+ - \mathbf{A}^- = \mathbf{0}$ on $\partial \mathcal{B}$, and zero on the boundary $\partial \Omega$ free space box (vacuum). (c) The crack phase-field is determined by Dirichlet-type boundary condition $d = 1$ on \mathcal{C} and Neumann-type boundary condition $\nabla d \cdot \mathbf{n} = 0$ on the full surface $\partial \mathcal{B}$.

$\partial_N \mathcal{B}$ denotes the outer domain boundary (where the traction imposed) and $\mathcal{C} \in \mathbb{R}^{\delta-1}$ is the crack boundary, as illustrated in Figure 2c. Therefore, we have three different domains required for the electromagnetically induced fracture to be used as follows:

Vacuum region: $\Omega \subset \mathbb{R}^\delta$, Solid region: $\mathcal{B} \subset \mathbb{R}^\delta$ and Damage region: $\mathcal{C} \in \mathbb{R}^{\delta-1}$.

The response of the fracturing solid at material points $\mathbf{x} \in \mathcal{B}$ at time $t \in \mathcal{T} = [0, T]$ is described by the displacement field $\mathbf{u}(\mathbf{x}, t)$ and the crack phase-field $d(\mathbf{x}, t)$ as

$$\mathbf{u} : \begin{cases} \mathcal{B} \times \mathcal{T} \rightarrow \mathbb{R}^\delta \\ (\mathbf{x}, t) \mapsto \mathbf{u}(\mathbf{x}, t) \end{cases} \quad \text{and} \quad d : \begin{cases} \mathcal{B} \times \mathcal{T} \rightarrow [0, 1] \\ (\mathbf{x}, t) \mapsto d(\mathbf{x}, t) \end{cases}. \quad (1)$$

Intact and fully fractured states of the material are characterized by $d(\mathbf{x}, t) = 0$ and $d(\mathbf{x}, t) = 1$, respectively. In order to derive the variational formulation, the following space is first defined. For an arbitrary $A \subset \mathbb{R}^\delta$, we set

$$\mathbf{H}^1(\mathcal{B}, A) := \left\{ v : \mathcal{B} \times \mathcal{T} \rightarrow A : v \in \mathbf{H}^1(A) \right\}. \quad (2)$$

We also denote the vector valued space $\mathbf{H}^1(\mathcal{B}, A) := [\mathbf{H}^1(\mathcal{B}, A)]^\delta$ and define

$$\mathcal{W}^u(\text{div}; \mathcal{B}) := \left\{ \mathbf{u} \in \mathbf{H}^1(\mathcal{B}, \mathbb{R}^\delta) : \mathbf{u} = \bar{\mathbf{u}} \text{ on } \partial_D \mathcal{B} \right\}, \quad (3)$$

and correspondingly for displacement test function, we have

$$\mathcal{W}_0^u(\text{div}; \mathcal{B}) := \left\{ \mathbf{u} \in \mathbf{H}^1(\mathcal{B}, \mathbb{R}^\delta) \right\}. \quad (4)$$

Concerning the crack phase-field, we set

$$\mathcal{W}^d := \mathbf{H}^1(\mathcal{B}) \quad \text{and} \quad \mathcal{W}_{d^n}^d(\text{div}; \mathcal{B}) := \left\{ d \in \mathbf{H}^1(\mathcal{B}, [0, 1]) : d \geq d^n \right\}, \quad (5)$$

where d^n is the damage value in a previous time instant. Note that $\mathcal{W}_{d^n}^d(\text{div}; \mathcal{B})$ is a non-empty, closed, and convex subset of \mathcal{W}^d and introduces the evolutionary character of the phase-field, incorporating an irreversibility condition in incremental form. Correspondingly the phase-field test function reads

$$\mathcal{W}_0^d(\text{div}; \mathcal{B}) := \left\{ d \in H^1(\mathcal{B}, [0, 1]) : d \geq 0 \right\}. \quad (6)$$

In order to formulate a wide variety of the failure mechanism of the electro- and magneto-active materials into the variational equations, two different sets of fields need to be introduced. To this end, the electric and magnetic primary fields are introduced:

$$\mathbf{E} : \left\{ \begin{array}{l} \Omega \times \mathcal{T} \rightarrow \mathbb{R}^\delta \\ (\mathbf{x}, t) \mapsto \mathbf{E}(\mathbf{x}, t) \end{array} \right. \quad \text{and} \quad \mathbf{H} : \left\{ \begin{array}{l} \Omega \times \mathcal{T} \rightarrow \mathbb{R}^\delta \\ (\mathbf{x}, t) \mapsto \mathbf{H}(\mathbf{x}, t) \end{array} \right. , \quad (7)$$

such that, the intensity fields (\mathbf{E}, \mathbf{H}) belong to the space:

$$\mathcal{S}^v(\text{curl}; \Omega) := \left\{ \mathbf{v} \in \mathbf{L}^2(\Omega, \mathbb{R}^\delta) : \nabla \times \mathbf{v} \in \mathbf{L}^2(\Omega, \mathbb{R}^\delta) \right\}, \quad (8)$$

along with their test function space as

$$\mathcal{S}_0^v(\text{curl}; \Omega) := \left\{ \mathbf{v} \in \mathcal{S}^v(\text{curl}; \Omega) : \mathbf{v} \times \mathbf{n} = 0 \in \mathbf{L}^2(\Omega, \mathbb{R}^\delta) \right\}. \quad (9)$$

The generalized fluxes conjugate to (7) for the electric and magnetic primary fields read:

$$\mathbf{D} : \left\{ \begin{array}{l} \Omega \times \mathcal{T} \rightarrow \mathbb{R}^\delta \\ (\mathbf{x}, t) \mapsto \mathbf{D}(\mathbf{x}, t) \end{array} \right. \quad \text{and} \quad \mathbf{B} : \left\{ \begin{array}{l} \Omega \times \mathcal{T} \rightarrow \mathbb{R}^\delta \\ (\mathbf{x}, t) \mapsto \mathbf{B}(\mathbf{x}, t) \end{array} \right. . \quad (10)$$

Correspondingly, the flux fields (\mathbf{D}, \mathbf{B}) are defined in the space:

$$\mathcal{S}^v(\text{div}; \Omega) := \left\{ \mathbf{v} \in \mathbf{L}^2(\Omega, \mathbb{R}^\delta) : \nabla \cdot \mathbf{v} \in \mathbf{L}^2(\Omega, \mathbb{R}^\delta) \quad \text{and} \quad \mathbf{v} = \bar{\mathbf{v}} \text{ on } \partial_D^0 \Omega \right\}, \quad (11)$$

and augmented with their test function space, as

$$\mathcal{S}_0^v(\text{div}; \Omega) := \left\{ \mathbf{v} \in \mathcal{S}^v(\text{div}; \Omega) : \mathbf{v} \cdot \mathbf{N} = 0 \text{ on } \partial_D \Omega := \partial_D^0 \Omega \cup \partial_D^1 \Omega \right\}. \quad (12)$$

Here, \mathbf{N} is the outward unit normal vector on the surface $\partial \Omega$, as illustrated in Figure 2.

These electric and magnetic primary fields and their fluxes describe the fundamental macroscopic fields governing all electromagnetic phenomena denoted as *Maxwell's equations*. These are described in detail in Section 2.2.2. To complete this section, we need to introduce the vector potential formulation of Maxwell's equations denoted as $\mathbf{A}(\mathbf{x}, t)$. Since, the *div* and *curl* operator are surjective, following [35, 36] the de Rham complex reads

$$\mathbb{R} \xrightarrow{id} H^1(\Omega) \xrightarrow{\text{grad}} H(\text{curl}, \Omega) \xrightarrow{\text{curl}} H(\text{div}, \Omega) \xrightarrow{\text{div}} L_2(\Omega) \xrightarrow{0} 0. \quad (13)$$

For a magnetic primary field $\mathbf{B} \in \mathcal{S}^v(\text{div}; \Omega)$ it holds

$$\nabla \cdot \mathbf{B} = 0 \quad \xrightarrow{\text{de Rham}} \quad \exists \mathbf{A} \in \mathcal{S}^v(\text{curl}; \Omega) : \nabla \times \mathbf{A} =: \mathbf{B}, \quad (14)$$

in which, \mathbf{A} denotes the magnetic vector potential. To summarize, we have following sets:

$$\begin{aligned} (\mathbf{u}, d) &\in \left(\mathcal{W}^u(\text{div}; \mathcal{B}), \mathcal{W}^d(\text{div}; \mathcal{B}) \right), & (\mathbf{E}, \mathbf{H}, \mathbf{A}) &\in \mathcal{S}^v(\text{curl}; \Omega) \\ (\mathbf{D}, \mathbf{B}) &\in \mathcal{S}^v(\text{div}; \Omega), \end{aligned} \tag{15}$$

and correspondingly it follows for their test functions:

$$\begin{aligned} (\delta \mathbf{u}, \delta d) &\in \left(\mathcal{W}_0^u(\text{div}; \mathcal{B}), \mathcal{W}_0^d(\text{div}; \mathcal{B}) \right), & (\delta \mathbf{E}, \delta \mathbf{H}, \delta \mathbf{A}) &\in \mathcal{S}_0^v(\text{curl}; \Omega), \\ (\delta \mathbf{D}, \delta \mathbf{B}) &\in \mathcal{S}_0^v(\text{div}; \Omega). \end{aligned} \tag{16}$$

2.2. Governing equations of the failure mechanism for magnetostrictive effects

In this section, we present a theoretical development associated with the failure mechanism of the ferromagnetic material based on the variational phase-field model by taking into account their fully coupled magneto-mechanical characteristics. This includes mechanical, electromagnetic, and fracture contributions to the model. Additionally, the transition rule from undamaged to fully damaged states is presented. This section is used as a departure point for Section 3 in which to formulate the variational framework for magnetostrictive-induced cracking is formulated.

2.2.1. Elastic contribution. The standard elastic energy density, so-called the effective strain energy density [37, 38] is expressed in terms of the scalar-valued function ψ_e . For isotropic materials, ψ_e is defined in terms of the strain tensor $\boldsymbol{\varepsilon}$. In our formulation, in order to preclude fracture in compression, a decomposition of the effective strain energy density into *damageable* and *undamageable* parts are employed. Thus, we perform additive decomposition of the strain tensor into *volume-changing* (volumetric) and *volume-preserving* (deviatoric) counterparts:

$$\boldsymbol{\varepsilon}(\mathbf{u}) = \boldsymbol{\varepsilon}^{vol}(\mathbf{u}) + \boldsymbol{\varepsilon}^{dev}(\mathbf{u}) \quad \text{with} \quad \boldsymbol{\varepsilon}(\mathbf{u}) := \frac{1}{2}(\nabla \mathbf{u} + \nabla^T \mathbf{u}), \tag{17}$$

where the volumetric strain is denoted as $\boldsymbol{\varepsilon}^{vol}(\mathbf{u}) := \frac{1}{3}(\boldsymbol{\varepsilon}(\mathbf{u}) : \mathbf{I})\mathbf{I}$ and the deviatoric strain is denoted as $\boldsymbol{\varepsilon}^{dev}(\mathbf{u}) := \mathbb{P} : \boldsymbol{\varepsilon}$. The fourth-order projection tensor $\mathbb{P} := \mathbb{I} - \frac{1}{3}\mathbf{I} \otimes \mathbf{I}$ is introduced to map the full strain tensor onto its deviatoric component. Therein, $\mathbb{I}_{ijkl} := \frac{1}{2}(\delta_{ik}\delta_{jl} + \delta_{il}\delta_{jk})$ is the fourth-order symmetric identity tensor.

Next we construct the mechanical BVP. The solid geometry \mathcal{B} is loaded by prescribed deformations $\bar{\mathbf{u}}$ and an external traction vector $\bar{\mathbf{t}}$ on the boundary, defined by time-dependent Dirichlet conditions and Neumann conditions as

$$\mathbf{u} = \bar{\mathbf{u}}(\mathbf{x}, t) \text{ on } \partial_D^u \mathcal{B} \quad \text{and} \quad \boldsymbol{\tau} \cdot \mathbf{n} = \bar{\mathbf{t}}(\mathbf{x}, t) \text{ on } \partial_N^u \mathcal{B}, \tag{18}$$

where \mathbf{n} is the outward unit normal vector on the surface $\partial_N \mathcal{B}$. The stress tensor $\boldsymbol{\tau}$ is the thermodynamic dual to the strain $\boldsymbol{\varepsilon}$.

The global mechanical form of the equilibrium equation for the solid body can be represented by a second-order PDE for the multi-field system as

$$\text{Div } \boldsymbol{\tau}(\mathbf{u}, \mathbf{B}, d) + \bar{\mathbf{b}} = \mathbf{0}, \tag{19}$$

which is valid for a quasi-static response and where denote $\bar{\mathbf{b}}$ is the prescribed body force.

2.2.2. Electromagnetic contribution. Maxwell's equations can principally express the macroscopic electromagnetic phenomena in a ferromagnetic material. These equations are related to the calculations of electromagnetic fields, including the electric and the magnetic fields with eddy currents (their corresponding fluxes)

$$\begin{aligned}
\text{Maxwell-Faraday law : } \quad \nabla \times \mathbf{E} &= -\frac{\partial \mathbf{B}}{\partial t} && \text{in } \Omega \times (0, T), \\
\text{Maxwell-Ampère law : } \quad \nabla \times \mathbf{H} &= \frac{\partial \mathbf{D}}{\partial t} + \mathbf{J} && \text{in } \Omega \times (0, T), \\
\text{Maxwell-Gauss law : } \quad \nabla \cdot \mathbf{D} &= \rho_0(d) && \text{in } \Omega \times (0, T), \\
\text{No magnetic monopole law : } \quad \nabla \cdot \mathbf{B} &= 0 && \text{in } \Omega \times (0, T),
\end{aligned} \tag{20}$$

where $\mathbf{E}(\mathbf{x}, t)$ and $\mathbf{H}(\mathbf{x}, t)$ are the electric and magnetic fields, $\mathbf{D}(\mathbf{x}, t)$ and $\mathbf{B}(\mathbf{x}, t)$ are the corresponding electric and magnetic flux densities, respectively, along with $\mathbf{J}(\mathbf{x}, t)$ that is the electric current density, and ρ is the electric charge density. In addition to these equations, there are constitutive equations that describe the macroscopic characteristics of a electromagnetic materials. These equations construct relations between the magnetic and electric flux densities and the magnetic and the electric fields

$$\mathbf{D} = \epsilon_0(d)\mathbf{E}, \quad \mathbf{B} = \mu_0(d)\mathbf{H} \quad \text{and} \quad \mathbf{J} = \sigma_0(d)\mathbf{E} + \mathbf{J}_s. \tag{21}$$

Remark 2.1. *We note that polarization is to be considered in the case of electromagnetic wave propagation that contains the electric and magnetic fields whose oscillations are perpendicular to the wave direction. The polarization is a feature of an electromagnetic wave that determines the geometrical orientation of the oscillations [39]. When an electromagnetic wave propagates in a homogeneous isotropic medium, the oscillations of electric and magnetic fields are perpendicular to each other and perpendicular to wave propagation's direction. The polarization expresses the direction of the electric field. Depending on the oscillation direction of the fields, there are two types of polarization, linear and circular the latter can be specified as the left circular and right circular polarization [40]. The polarization effect is regarded in Maxwell's equation by modifying (21) in terms of the electric magnetic field \mathbf{D} as [12]*

$$\mathbf{D} = \epsilon_0(d)\mathbf{E} + \mathbf{P}, \tag{22}$$

where \mathbf{P} represents the polarization of the electromagnetic wave propagation. In our work we further assume \mathbf{P} has negligible effect, thus $\mathbf{P} = \mathbf{0}$. Therefore, this effect is not anymore take into account in our study.

Here, \mathbf{J}_s denotes the specific current density. Also, material constants ϵ_0 , μ_0 , and σ_0 represent the permittivity, the permeability, and the conductivity of the medium, respectively. We further note that ϵ_0 , μ_0 , and σ_0 are piecewise smooth, real, bounded, and positive and may vary in different Cartesian coordinates. We need to mention that dependency of these variables to the crack phase-field is further elaborated in Section

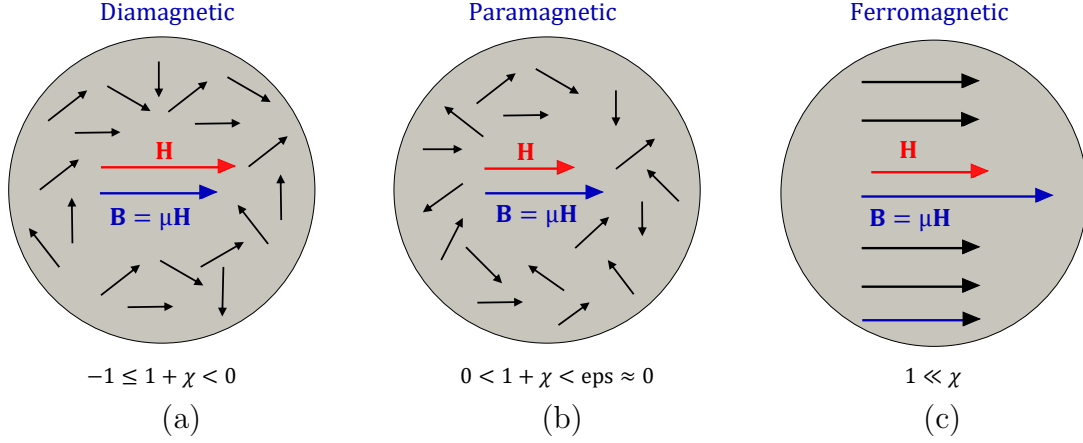


Figure 3: Partial alignment of the magnetic moments in the presence of the external magnetic field for classified based on relative magnetic permeability of materials, (a) diamagnetic with $-1 \leq 1 + \chi < 0$, (b) for paramagnetic with $0 \leq 1 + \chi < \text{eps}$, and (c) for ferromagnetic $1 \ll \chi$ in parallel orientation of magnetic moment in the presence of the external magnetic field.

2.2.4. Thus, we have for every $\mathbf{x} \in \Omega$:

$$\begin{aligned}
 0 < \epsilon_{0,min} < \epsilon_0 < \epsilon_{0,max} < \infty, \\
 0 < \mu_{0,min} < \mu_0 < \mu_{0,max} < \infty, \\
 0 < \sigma_{0,max} < \infty.
 \end{aligned}
 \tag{23}$$

Additional to (20) and (21), the Dirichlet boundary condition are for the electric field and magnetic vector potential:

$$\mathbf{E} = \bar{\mathbf{E}}(\mathbf{x}, t) \text{ on } \partial_D^1 \Omega \text{ and } \mathbf{A} = \bar{\mathbf{A}}(\mathbf{x}, t) \text{ on } \partial_D^1 \Omega.
 \tag{24}$$

On the boundary of the free space, outer Dirichlet and Neumann boundary conditions have to be satisfied as:

$$\bar{\mathbf{A}} = \mathbf{0} \text{ on } \partial_D^0 \Omega \text{ and } \nabla \bar{\mathbf{A}} \cdot \mathbf{N} = \mathbf{0} \text{ on } \partial_D^0 \Omega,
 \tag{25}$$

respectively, such that:

$$\lim_{\mathbf{x} \rightarrow \infty} \bar{\mathbf{A}}(\mathbf{x}, t) \rightarrow \mathbf{0}.$$

In the case of the magnetized material, the constitutive relation between magnetic flux \mathbf{H} and magnetic field \mathbf{B} needs to be further modified. This adjustment will help to accommodate our proposed formulation of a magneto-mechanical problem of fracturing solids. To do so, we describe three common types of macroscopic magnetization responses as follows:

- **Diamagnetic.** These types of materials are those which become weakly magnetized when they are affected by an external magnetic field. The tendency of magnetization for paramagnetic materials is to move in the direction of a strong magnetic field towards weak parts of the external magnetic field [41]. So, diamagnetic materials are magnetized in the opposite direction of the external magnetic field. Moreover, these material present no magnetic hysteresis.

- **Paramagnetic.** Similar to the diamagnetic response, this type of material becomes weakly magnetized. Unlike diamagnetic materials, the tendency of magnetization for paramagnetic materials is to move in the direction of weak magnetic fields to strong ones [41]. So, paramagnetic materials are magnetized in the direction of the external magnetic field. Here, small magnetic hysteresis could be observed .
- **Ferromagnetic.** This class of magnetic materials is described through a permanent magnetization effect and mainly has a profound response to magnetic fields. These materials are characterized by a highly nonlinear response in which magnetic hysteresis typically occurs [42].

To formulate a different class of magnetic material, the constitutive relation between \mathbf{B} and \mathbf{H} is described through:

$$\mathbf{B} = \boldsymbol{\mu} \cdot \mathbf{H} \quad \text{with} \quad \boldsymbol{\mu} = \mu_0(\mathbf{I} + \boldsymbol{\chi}), \quad (26)$$

in which magnetic susceptibility $\boldsymbol{\chi}$ (as a dimensionless quantity), measures the degree of magnetization response of material if there is an external magnetic field leading to:

$$\mathbf{M} = \boldsymbol{\chi} \cdot \mathbf{H} \quad \text{with} \quad \boldsymbol{\chi} = \frac{\partial \mathbf{M}}{\partial \mathbf{H}}. \quad (27)$$

The term $\mathbf{I} + \boldsymbol{\chi}$ in (26) typically refers to the *relative magnetic permeability* of materials. Thus, the coupling of (26) and (27) results in:

$$\mathbf{B} = \mu_0(\mathbf{I} + \boldsymbol{\chi}) : \mathbf{H} = \mu_0(\mathbf{H} + \mathbf{M}). \quad (28)$$

On the basis of the magnitude of magnetic susceptibility $\|\boldsymbol{\chi}\|_2$ in (28), magnetized material is classified into the above mentioned:

$$\begin{aligned} \text{Diamagnetic:} \quad & -1 \leq \|\boldsymbol{\chi}\|_2 < 0, \\ \text{Paramagnetic:} \quad & 0 < \|\boldsymbol{\chi}\|_2 < \text{eps} \approx 0, \\ \text{Ferromagnetic:} \quad & \|\boldsymbol{\chi}\|_2 \gg 1, \end{aligned} \quad (29)$$

see Figure 3. In our case, we use the magnetic susceptibility as an isotropic tensor for the ferromagnetic response: $\boldsymbol{\chi} = \chi_0 \mathbf{I}$ with $\chi_0 \gg 1$, which is valid for a variety of amorphous solids or materials with a uniform crystal structure [43]. Since \mathbf{B} is solenoidal (divergence-free) according to Maxwell's equations, we know through (14) that \mathbf{B} must be the curl of the magnetic vector potential field \mathbf{A} , so $\mathbf{B} = \nabla \times \mathbf{A}$. In a common way, the electromagnetic fields, $\mathbf{E}(\mathbf{x}, t)$, $\mathbf{H}(\mathbf{x}, t)$, $\mathbf{D}(\mathbf{x}, t)$ and $\mathbf{B}(\mathbf{x}, t)$ are presumed to be time-harmonic. It means that the fields can harmonically oscillate with a single frequency ω . In such cases, they can be written as

$$\begin{aligned} \mathbf{E}(\mathbf{x}, t) &= \exp(-i\omega t) \mathbf{E}(\mathbf{x}, \omega), \\ \mathbf{H}(\mathbf{x}, t) &= \exp(-i\omega t) \mathbf{H}(\mathbf{x}, \omega), \\ \mathbf{J}_s(\mathbf{x}, t) &= \exp(-i\omega t) \mathbf{J}_s(\mathbf{x}, \omega). \end{aligned} \quad (30)$$

The first and the second-order derivatives are

$$\begin{aligned} \frac{\partial \mathbf{E}(\mathbf{x}, t)}{\partial t} &= -i\omega \mathbf{E}(\mathbf{x}, t), & \frac{\partial^2 \mathbf{E}(\mathbf{x}, t)}{\partial t^2} &= -\omega^2 \mathbf{E}(\mathbf{x}, t), \\ \frac{\partial \mathbf{H}(\mathbf{x}, t)}{\partial t} &= -i\omega \mathbf{H}(\mathbf{x}, t), & \frac{\partial^2 \mathbf{H}(\mathbf{x}, t)}{\partial t^2} &= -\omega^2 \mathbf{H}(\mathbf{x}, t), \\ \frac{\partial \mathbf{J}_s(\mathbf{x}, t)}{\partial t} &= -i\omega \mathbf{J}_s(\mathbf{x}, t), & \frac{\partial^2 \mathbf{J}_s(\mathbf{x}, t)}{\partial t^2} &= -\omega^2 \mathbf{J}_s(\mathbf{x}, t). \end{aligned} \quad (31)$$

Therefore, the time-harmonic Maxwell's equations are obtained by substituting (30) and (21) into (20)

$$\begin{cases} \nabla \times \mathbf{E}(\mathbf{x}, t) = i\omega\mu_0 \mathbf{H}(\mathbf{x}, t) & \text{in } \Omega \times (0, T) \\ \nabla \times \mathbf{H}(\mathbf{x}, t) = -i\omega \left(\epsilon_0 + i\frac{\sigma_0}{\omega} \right) \mathbf{E}(\mathbf{x}, t) + \mathbf{J}_s(\mathbf{x}, t) & \text{in } \Omega \times (0, T) \end{cases}. \quad (32)$$

We now take a curl function, i.e., $\nabla \times$, from the first equation of (32), which results in:

$$\nabla \times \mathbf{H}(\mathbf{x}, t) = \nabla \times \left(\frac{1}{i\omega\mu_0} \nabla \times \mathbf{E}(\mathbf{x}, t) \right). \quad (33)$$

Next, we use the curl function from the second expression of (32) and with (33), we obtain the equation for electric field $\mathbf{E}(\mathbf{x}, t)$ as

$$\nabla \times \left(\frac{1}{\mu_0} \nabla \times \mathbf{E}(\mathbf{x}, t) \right) - \omega^2 \left(\epsilon_0 + i\frac{\sigma_0}{\omega} \right) \mathbf{E}(\mathbf{x}, t) = i\omega \mathbf{J}_s(\mathbf{x}, t). \quad (34)$$

In a similar manner, we can derive the equation for the magnetic field $\mathbf{H}(\mathbf{x}, t)$ by taking the curl from the second expression of (32) as

$$\nabla \times (\nabla \times \mathbf{H}(\mathbf{x}, t)) = -i\omega \left(\epsilon_0 + i\frac{\sigma_0}{\omega} \right) \nabla \times \mathbf{E}(\mathbf{x}, t) + \nabla \times \mathbf{J}_s(\mathbf{x}, t), \quad (35)$$

where $\nabla \times \mathbf{E}(\mathbf{x}, t) = i\omega\mu_0 \mathbf{H}(\mathbf{x}, t)$. Therefore, we obtain

$$\nabla \times (\nabla \times \mathbf{H}(\mathbf{x}, t)) - \omega^2 \mu_0 \left(\epsilon_0 + i\frac{\sigma_0}{\omega} \right) \mathbf{H}(\mathbf{x}, t) = \nabla \times \mathbf{J}_s(\mathbf{x}, t). \quad (36)$$

The time-domain vector wave equations in terms of the electric field $\mathbf{E}(\mathbf{x}, t)$ and the magnetic field $\mathbf{H}(\mathbf{x}, t)$ are further simplified by substituting (31) into (34) and (36). This yields:

$$\begin{cases} \epsilon_0 \frac{\partial^2 \mathbf{E}}{\partial t^2} + \sigma_0 \frac{\partial \mathbf{E}}{\partial t} + \nabla \times \left(\frac{1}{\mu_0} \nabla \times \mathbf{E} \right) = -\frac{\partial \mathbf{J}_s}{\partial t} & \text{in } \Omega \times (0, T) \\ \epsilon_0 \frac{\partial^2 \mathbf{H}}{\partial t^2} + \sigma_0 \frac{\partial \mathbf{H}}{\partial t} + \nabla \times \left(\frac{1}{\mu_0} \nabla \times \mathbf{H} \right) = \frac{1}{\mu_0} \nabla \times \mathbf{J}_s & \text{in } \Omega \times (0, T) \end{cases}. \quad (37)$$

In order to demonstrate the modeling capacity of (37), a representative simulation is presented in Figure 4. In this boundary-value problem, the evolution of the electric field

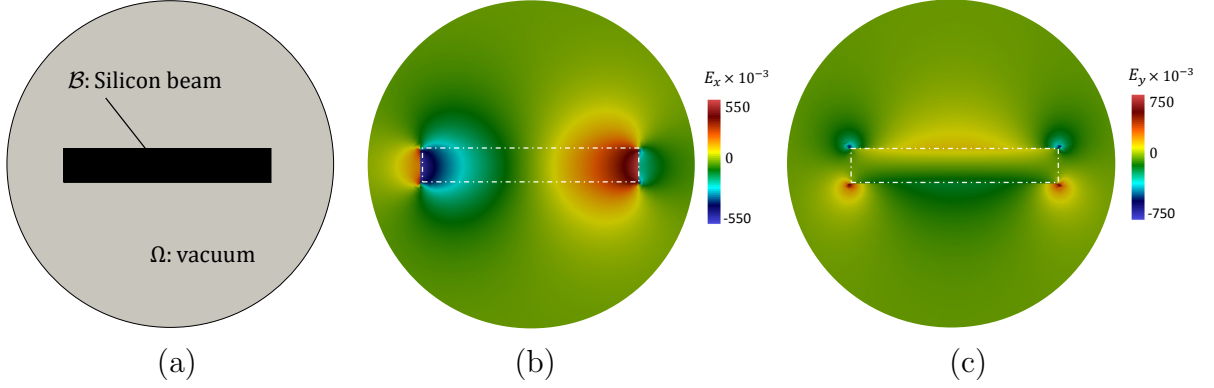


Figure 4: The geometry of BVP, and the the representation of the x - and y - component of the electric field \mathbf{E} .

\mathbf{E} is represented in the x and y directions under the variation of the specific current \mathbf{J}_s . In this example, the specific current \mathbf{J}_s is defined as a bi-linear function of the nodal coordinates and time. As a boundary condition, the electric field is set to $\mathbf{E} = \mathbf{0}$ at the boundaries of the vacuum. The results show that the variation of the electric field is symmetric along the x and y directions as the electric specific current is uniformly applied on the silicon beam. In fact, this is expected due to symmetric response of electric field imposed to domain.

Next, we reduce (37) toward Maxwell's equations in terms of vector potential. The Maxwell-Faraday law in (20), based on magnetic vector potential $\mathbf{A}(\mathbf{x}, t)$ given in (14), is then related to electric field through:

$$\nabla \times \mathbf{E} = -\frac{\partial(\nabla \times \mathbf{A})}{\partial t} \rightarrow \exists \Phi(\mathbf{x}, t) : -\nabla\Phi = \mathbf{E} + \frac{\partial\mathbf{A}}{\partial t}. \quad (38)$$

Here, $\Phi(\mathbf{x}, t)$ is so-called the electric potential, see for a detailed discussion [44, 45]. From the mathematical point of view, the homogeneous Maxwell equations for Maxwell-Faraday law (20)₁, and Maxwell-Ampère law in (20)₂ results in the existence set of (\mathbf{A}, Φ) , and thus implies (38). We refer interested readers to [46] for more details. Considering Maxwell-Ampère law in (20), and constitutive equations (21), yields:

$$\frac{1}{\mu_0} \nabla \times \mathbf{B} = \epsilon_0(d) \frac{\partial \mathbf{E}}{\partial t} + \mathbf{J} \quad (39)$$

that is

$$\nabla \times \left(\frac{1}{\mu_0} \nabla \times \mathbf{A} \right) = -\epsilon_0(d) \left[\frac{\partial \nabla \Phi}{\partial t} + \frac{\partial^2 \mathbf{A}}{\partial t^2} \right] - \sigma_0(d) \left[\nabla \Phi + \frac{\partial \mathbf{A}}{\partial t} \right] + \mathbf{J}_s \quad (40)$$

where (38) and (21) are used. Next, we assume that for a time dependent magnetic vector potential $\mathbf{A}(\mathbf{x}, t)$, and the electric potential $\Phi(\mathbf{x}, t)$, we have:

$$\text{Div} \mathbf{A} + \mu_0 \epsilon_0 \frac{\partial \Phi(\mathbf{x}, t)}{\partial t} = 0, \quad (41)$$

which is the so-called Lorenz gauge condition [47, 45]. Thus, (40) together with (41) reads:

$$\boxed{\frac{1}{\mu_0} \nabla^2 \mathbf{A} = \epsilon_0(d) \left[\frac{\partial^2 \mathbf{A}}{\partial t^2} \right] + \sigma_0(d) \left[\nabla \Phi + \frac{\partial \mathbf{A}}{\partial t} \right] - \mathbf{J}_s} \quad (42)$$

Here, the identity $\nabla \times \nabla \times \mathbf{A} = \nabla(\text{Div} \mathbf{A}) - \nabla^2 \mathbf{A}$ is used.

We note that, the magnetic potential $A(x, t)$ as a solution of (42) is related to crack parameter d by PDE coefficients. So, the permittivity, the permeability, and the conductivity of the medium $(\epsilon_0(d), \mu_0(d), \sigma_0(d))$ are function of d , see Section 2.2.4.

The setting presented in [48] constitutes the starting point to formulate the mechanical response within the electromagnetic analysis where the electric scalar potential $\nabla\Phi$ in (42) is a *given quantity*. Following [48, 49], the magneto-static state $\nabla\Phi$ has the direction orthogonal to the x - y plane, i.e., $\nabla\Phi(t) = [0, 0, \nabla\Phi_0(t)]$, where $\Phi_0(t)$ is the pulse power supply parameter which is approximated as:

$$\nabla\Phi_0(t) = a + b e^{-ct}. \quad (43)$$

It is determined as a function of the constants a, b and c [48, 49]². In all our representative numerical examples in Section 4, these values are set as $a = -1 \times 10^{-3}$ V/m, $b = -1 \times 10^{-3}$ V/m, and $c = 1 \times 10^{-2}$ s⁻¹.

2.2.3. Fracture contribution. In the smeared fracture framework, a sharp crack interface denoted by \mathcal{C} for satisfying the continuity of the crack topology is further regularized, which is denoted as \mathcal{C}_l as outlined [28]. To govern a regularized fracture surface \mathcal{C}_l , it is required to incorporate a continuous field variable – the so-called order parameter – denoted by d , which differentiates between multiple physical phases within a given system through a smooth transition. In the context of fracture, such an order parameter (termed the crack phase-field) describes the smooth transition between the fully broken ($d = 1$) and intact material phases ($d = 0$), thereby approximating the sharp crack discontinuity. This geometrical perspective is in agreement with the framework of [50], which was conceived as a Γ -convergence regularization of the variational approach to Griffith fracture [51]. A variety of research studies have recently extended the phase-field approach to fracture toward the cohesive-frictional materials [52] including thermal effects [53, 54, 55], ductile failure [56, 57, 58], hydraulic fracture [59, 60, 61], stochastic analysis [62, 63, 64, 65], degradation of the fracture toughness [57], topology optimization [66], and multi-scale

²Clearly, the representation on electric scalar potential given in (43) can be derived through Maxwell's equations, as well, and *not* as a given quantity. By means of Maxwell-Gauss law in (20)₃, and constitutive equation (21)₁, we have:

$$-\nabla^2\Phi - \nabla \cdot \left(\frac{\partial \mathbf{A}}{\partial t} \right) = -\frac{\rho_0(d)}{\epsilon_0(d)} \quad (44)$$

where (38) is used. Then, by imposing Lorenz gauge condition in (44), results in the wave-like equation by:

$$c_\Phi^2 \frac{\partial^2 \Phi}{\partial t^2} = \nabla^2 \Phi + f_\Phi \quad \text{in } \Omega \times (0, T), \quad (45)$$

with

$$f_\Phi = -\frac{\rho_0(d)}{\epsilon_0(d)} \quad \text{and} \quad c_\Phi^2 = \mu_0(d)\epsilon_0(d) \quad (46)$$

The the electric potential PDE given (45) is a linear second-order differential equation with the variable $\Phi \in H^1(\Omega, \mathbb{R})$ represents the wave-like propagates in the free space with the constant speed of c_Φ , and f_Φ states the source of the wave propagation. Thus, set of equations (42) and (45) are replaced by (37) to represent the Maxwell's equations in terms of vector potential.

approach [67, 38, 68, 69], and electro-mechanical approach [70, 71, 72] among others. In this manuscript, for the case of isotropic materials, the regularized functional is given by

$$\mathcal{C}_l(d) = \int_{\mathcal{B}} \gamma(d, \nabla d) \, d\mathcal{B}, \quad (47)$$

with positiveness for crack dissipation as:

$$\frac{d}{dt} \mathcal{C}_l(d) \geq 0. \quad (48)$$

In line with standard phase-field models, a general surface density function for the isotropic part $\gamma(d, \nabla d)$ is defined as

$$\gamma(d, \nabla d) := \frac{1}{c_d} \left(\frac{f(d)}{l_d} + \frac{l_d}{2} \nabla d \cdot \nabla d \right) \quad \text{with} \quad c_d := 4 \int_0^1 \sqrt{\omega(b)} \, db, \quad (49)$$

where $\omega(d)$ is a monotonic and continuous *local fracture energy function* such that $\omega(0) = 0$ and $\omega(1) = 1$. A variety of suitable choices for $\omega(d)$ are available in the literature [73, 74, 75]. Here, the widely adopted linear and quadratic formulations are considered, which yield, models with and without an elastic stage, respectively. Specifically, we define

$$f(d) := \begin{cases} d & \implies c_d = 8/3 & \text{model with an elastic stage,} \\ d^2 & \implies c_d = 2 & \text{model without an elastic stage.} \end{cases} \quad (50)$$

Following [76], the local evolution of the crack phase-field equation in the domain \mathcal{B} is:

$$\boxed{[d - l_d^2 \Delta d] + \eta_d \dot{d} + (1 - \kappa)(d - 1)\mathcal{H} = 0,} \quad (51)$$

augmented with its homogeneous Neumann boundary conditions, i.e., $\nabla d \cdot \mathbf{n} = 0$ on $\partial\mathcal{B}$. Following [37, 38], the small residual scalar $0 < \kappa \ll 1$ is introduced to prevent numerical instabilities, which states the *third* equation in the coupled system. Additionally, the damage viscosity material parameter denoted by $\eta_d \geq 0$ is used to characterize the viscosity term of the crack propagation. The maximum absolute value for the crack driving state function denoted by \mathcal{D} is defined by the crack driving force \mathcal{H} , which reads

$$\mathcal{H} = \max_{s \in [0, t]} \mathcal{D}(\mathbf{x}, s) \geq 0, \quad (52)$$

that accounts for the irreversibility of the crack phase-field evolution by filtering out a maximum value of \mathcal{D} . We define the crack driving state function in Section 3.

In summary, following formulation has to be solved for three-field $(\mathbf{u}, d, \mathbf{A})$ multi-physics problem.

Formulation 2.1 (Strong form of the Euler-Lagrange equations). *Let $\epsilon_0, \sigma_0, \mu_0, G_c, K$, and μ be given with the initial conditions $\mathbf{u}^0 = \mathbf{u}(\mathbf{x}, 0)$, $d^0 = d(\mathbf{x}, 0)$, and $\mathbf{A}^0 = \mathbf{A}(\mathbf{x}, 0)$. For the loading increments $n = 1, 2, \dots, N$, we solve a displacement equation where we seek $\mathbf{u} := \mathbf{u}^n : \mathcal{B} \rightarrow \mathbb{R}^\delta$ such that*

$$\begin{aligned} -\operatorname{div}(\boldsymbol{\tau}) &= \mathbf{0} && \text{in } \mathcal{B}, \\ \mathbf{u} &= \bar{\mathbf{u}} && \text{on } \partial_D \mathcal{B}, \\ \boldsymbol{\tau} \cdot \mathbf{n} &= \bar{\mathbf{t}} && \text{on } \partial_N \mathcal{B}, \end{aligned}$$

in terms of the stress tensor $\boldsymbol{\tau}$ defined in (79) and the given displacement field $\bar{\mathbf{u}}$. The phase-field system consists of four parts: the PDE, the inequality constraint and a compatibility condition along with the Neumann-type boundary conditions. Find $d := d^n : \mathcal{B} \rightarrow [0, 1]$ such that

$$\begin{aligned} (1 - \kappa)(1 - d)\mathcal{H}(I_1, I_2, t) - [d - l_d^2 \Delta d] &= \eta_d \dot{d} & \text{in } \mathcal{B}, \\ \dot{d} &\geq 0 & \text{in } \mathcal{B}, \end{aligned}$$

in terms of the crack driving force given (83), along with $\nabla d \cdot \mathbf{n} = 0$ on $\partial\Omega$. along with a second-order hyperbolic problem for the following magnetic vector potential. Find $\mathbf{A} := \mathbf{A}^n : \Omega \rightarrow \mathbb{R}^\delta$ such that

$$\frac{1}{\mu_0} \nabla^2 \mathbf{A} = \epsilon_0(d) \left[\frac{\partial^2 \mathbf{A}}{\partial t^2} \right] + \sigma_0(d) \left[\nabla \Phi + \frac{\partial \mathbf{A}}{\partial t} \right] - \mathbf{J}_s \quad \text{in } \Omega.$$

where the Lorenz gauge condition is considered.

2.2.4. Transition structure from undamaged to fully damaged states. In this section, we provide a transition rule to connect the transition between the intact (solid) region and the fracture domain. In fact, the coupling of electromagnetic response to the crack phase field is achieved by introducing constitutive functions, which are characterized by degraded related material constants. Following [77], two state functions need to be defined. The first set of the formulation is denoted as $\mathbf{P}^s(\mathbf{x}) \in \mathcal{B} \setminus \mathcal{C}_l$, which exists in the solid part of materials to describe the degradation of elastic stored contribution in energy. In order to extend $\mathbf{P}^s(\mathbf{x})$ to the entire domain \mathcal{B} , we define $\widehat{\mathbf{P}}^s(\mathbf{x}, d)$ as:

$$\mathbf{P}^s(\mathbf{x}) \in \mathcal{B} \setminus \mathcal{C}_l \quad \longrightarrow \quad \widehat{\mathbf{P}}^s(\mathbf{x}, d) \in \mathcal{B} \quad \text{with} \quad \widehat{\mathbf{P}}^s(\mathbf{x}, d) = \mathcal{G}^s(d) \mathbf{P}^s(\mathbf{x}), \quad (53)$$

with decreasing crack phase-field. Here, $\mathcal{G}^s(d)$ has a descending order in terms of the crack phase-field. This set of functions can be used to describe, e.g., heat permeability, fluid permeability, or in our study, the permittivity and the permeability of the ferromagnetic medium. More precisely, all sets of solid response are a subset of $\widehat{\mathbf{P}}^s(\mathbf{x}, d)$ such that in the limit case this state function $\widehat{\mathbf{P}}^s(\mathbf{x}, d \rightarrow 0) \rightarrow \mathbf{P}^s(\mathbf{x})$ thus resembling classical constitutive state variables for the solid response.

The second set of the formulation is denoted as $\mathbf{P}^d(\mathbf{x}) \in \mathcal{C}_l$, which exists in the damaged domain to describe the fractured constitutive response. To further extend $\mathbf{P}^f(\mathbf{x})$ to the entire domain, we define:

$$\mathbf{P}^f(\mathbf{x}) \in \mathcal{C}_l \quad \longrightarrow \quad \widehat{\mathbf{P}}^f(\mathbf{x}, d) \in \mathcal{B} \quad \text{with} \quad \widehat{\mathbf{P}}^f(\mathbf{x}, d) = \mathcal{G}^f(d) \mathbf{P}^f(\mathbf{x}), \quad (54)$$

with increasing crack phase-field. Here, $\mathcal{G}^f(d)$ has an ascending order in terms of the crack phase-field, which has a inverse effect of $\mathcal{G}^s(d)$ into the constitutive response. As a result, we have the following properties:

$$\begin{aligned} \text{solid part:} \quad & \mathcal{G}^s(d \rightarrow 0) \rightarrow 1, \quad \mathcal{G}^s(d \rightarrow 1) \rightarrow 0 \quad \text{with} \quad \partial_d \mathcal{G}^s \leq 0 \\ \text{fracture part:} \quad & \mathcal{G}^f(d \rightarrow 0) \rightarrow 0, \quad \mathcal{G}^f(d \rightarrow 1) \rightarrow 1 \quad \text{with} \quad \partial_d \mathcal{G}^f \geq 0 \end{aligned} \quad (55)$$

Thus, $\mathcal{G}^f(d = 0)$ is zero in the solid domain, while $\mathcal{G}^s(d = 1)$ is zero in the fracture domain. In this contribution, we propose the following formulation for $\mathcal{G}^s(d)$ and $\mathcal{G}^f(d)$ of order m for a given set of parameters (c_1, c_2) , for the solid contribution as:

$$\mathcal{G}^s(d) = \left(\frac{c_2 - d}{c_2 - c_1} \right)^m \quad \text{with} \quad \mathcal{G}^s(d) = 1 \quad \text{if} \quad d < c_1 \quad \text{and} \quad \mathcal{G}^s(d) = 0 \quad \text{if} \quad d > c_2, \quad (56)$$

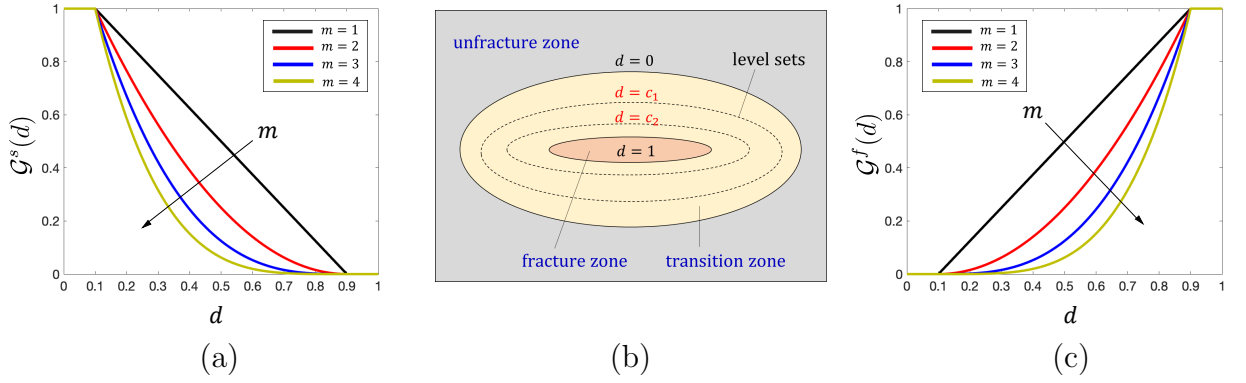


Figure 5: (a) Degradation function for solid material denoted as $\mathcal{G}^s(d)$ (b) with representation the fracture domain if $d > c_2$ and unfracture domain if $d < c_1$, and (c) Degradation function for regularized crack phase-field $\mathcal{G}^f(d)$. Here, we used $m = \{1, 2, 3, 4\}$ with adjustable constants $(c_1, c_2) = (0.1, 0.9)$.

and the fracture contribution as:

$$\mathcal{G}^f(d) = \left(\frac{d - c_1}{c_2 - c_1} \right)^m \quad \text{with} \quad \mathcal{G}^f(d) = 0 \quad \text{if} \quad d < c_1 \quad \text{and} \quad \mathcal{G}^f(d) = 1 \quad \text{if} \quad d > c_2, \quad (57)$$

which is in line properties (55). In the following numerical study we use the quadratic order for both $\mathcal{G}^s(d)$ and $\mathcal{G}^f(d)$, so $m = 2$, and we further set $(c_1, c_2) = (0.1, 0.9)$, see Figure 5.

Remark 2.2. For the linear order $m = 1$ our proposed degradation function is similar with linear indicator functions given in [78], and for the quadratic order $m = 2$ with constants $(c_1, c_2) = (0, 1)$ it mimics quadratic indicator functions given in [77]. Hence, (56) and (57) are generalized formulation versus [77] and [78].

To denote the effect of the magnetization-induced cracking in the material, we propose an anisotropic electromagnetic material constants in Maxwell's equations. This provides a simple constitutive assumption for an electromagnetic material to represent the transition rule. These constants can be re-formulated through crack phase-field d . Thus, by means of state functions for solid and fracture regions described in (56) and (57), the definition of the electromagnetic material constants is then proposed as follows:

$$\begin{aligned} \text{permeability:} \quad & \mu_0(d) = \mathcal{G}^s(d)\mu_0^s + \mathcal{G}^f(d)\mu_0^f, \\ \text{permittivity:} \quad & \epsilon_0(d) = \mathcal{G}^s(d)\epsilon_0^s + \mathcal{G}^f(d)\epsilon_0^f, \\ \text{conductivity:} \quad & \sigma_0(d) = \mathcal{G}^s(d)\sigma_0^s + \mathcal{G}^f(d)\sigma_0^f, \\ \text{electric charge density:} \quad & \rho_0(d) = \mathcal{G}^s(d)\rho_0^s + \mathcal{G}^f(d)\rho_0^f. \end{aligned} \quad (58)$$

The first term in the anisotropic materials expression in (58) for a set of $(\mu_0, \epsilon_0, \sigma_0, \rho_0)$ can be indicated as a classical isotropic intrinsic material property for permeability, permittivity, conductivity, and electric charge density, respectively. Also, in general, the number of constants $(\mu_0^f, \epsilon_0^f, \sigma_0^f, \rho_0^f)$ are much less than material constants corresponding to solid

parts and greater than the number of constants describing vacuum counterparts. We note that in our study, the second term in (58) is also a material property, which one can relate to classical crack jump, e.g., in failure mechanics of a thermo-elastic solid in [77], or in hydraulic fracturing of fluid-saturated porous media [79, 64, 65].

3. Energy quantities and variational principles

To outline the variational formulation setting, it suffices to define the constitutive energy density functions W_{elas} , W_{mag} , W_{mos} , and W_{frac} corresponds to elastic, magnetostrictive, magnetization, and fracture contributions, respectively. These energy quantities lead to establishing the multi-field evolution problem in terms of the primary fields described in Section 2. To this end, the related constitutive relations are provided. On this basis, a coupling between the magnetostriction and the mechanics is formulated to investigate the mechanical deformation of materials under the magnetic forces. Furthermore, the cracking response under the magnetic forces is examined. The energetic crack driving force is governed by the coupling magneto-mechanical effects under the magneto-static state. We extend the variational formulations of the coupled multi-physics system within the magneto-mechanical formulation of fracturing solids. We complete this section by providing a compact algorithmic framework for magnetostrictive-induced cracking.

3.1. Constitutive functions

The coupled BVP is formulated by introducing three specific fields for magneto-mechanically-induced cracking of the magneto-active materials

$$\text{Global Primary Fields : } \mathfrak{U} := \{\mathbf{u}, d, \mathbf{A}\}. \quad (59)$$

Here, \mathbf{u} is the displacement (mechanical deformation), \mathbf{A} denotes the magnetic vector potential field, and d is the crack phase-field ($0 \leq d \leq 1$). From the numerical implementation standpoint, to guarantee $0 \leq d \leq 1$ holds, we project $d > 1$ to 1 and $d < 0$ to 0 to avoid unphysical crack phase-field solution [61]. The constitutive equations for the magnetostrictive phase-field fracture are written in terms of the set

$$\text{Constitutive State Variables : } \mathfrak{C} := \{\boldsymbol{\varepsilon}, d, \nabla d, \mathbf{B}\}, \quad (60)$$

representing a combination of a magneto-mechanical model through the Maxwell's equation and a first-order gradient damage model.

3.1.1. Energy quantities. A pseudo-energy density per unit volume is then defined as $W := W(\mathfrak{C})$, which is additively decomposed into an elastic contribution W_{elas} , a magnetization contribution W_{mag} , a magnetostriction contribution W_{mos} , and a (regularized) fracture contribution W_{frac} through:

$$W(\mathfrak{C}) := W_{elas}(\boldsymbol{\varepsilon}, d) + W_{mag}(\boldsymbol{\varepsilon}, \mathbf{B}, d) + W_{mos}(\boldsymbol{\varepsilon}, \mathbf{B}, d) + W_{frac}(d, \nabla d). \quad (61)$$

We note that $W(\mathfrak{C})$ is a state function that contains both energetic and dissipative contributions. With this function at hand, a pseudo potential energy functional can be

constructed

$$\begin{aligned}\mathcal{E}(\mathbf{u}, \mathbf{A}, d) &:= \int_{\Omega} W(\boldsymbol{\epsilon}) \, d\mathbf{x} \\ &= \int_{\mathcal{B}} \left[W_{elas}(\boldsymbol{\epsilon}, d) + W_{frac}(d, \nabla d) \right] \, d\mathbf{x} + \int_{\Omega} \left[W_{mag}(\boldsymbol{\epsilon}, \mathbf{B}, d) + W_{mos}(\boldsymbol{\epsilon}, \mathbf{B}, d) \right] \, d\mathbf{x}.\end{aligned}\tag{62}$$

All these counterparts will be elaborated in following sections.

3.1.2. Magnetization contribution. Magnetization is defined as a vector field describing the density of permanent or induced magnetic *dipole moments* in a magnetic material [80]. The magnetic dipole moments are caused by either microscopic electric currents resulting from the motion of electrons in atoms or the spin of the electrons or the nuclei. In a magnetic field, a strong magnetization response is observed in ferromagnetic materials. Any ferromagnetic material is capable of being magnetized in the absence of an external magnetic field and becoming a permanent magnet. It is not necessary that the magnetization distributes uniformly within the material, so the material may present an anisotropic response when subjected to the magnetization effect. Ferromagnetic materials have inherent strong coupled magnetic and mechanical behavior, so the material magnetization affects the stress response of material via magnetostriction phenomenon, and the stress state of the material also affects magnetization via inverse magnetostriction [81]. Following [16], the magnetization density function is formulated as:

$$W_{mag}(I_1, I_4, d) := \frac{1}{2} \sum_{i=0}^4 \frac{g_i(I_1)}{i+1} \left(\frac{I_4}{B_{ref}^2} \right)^i I_4, \tag{63}$$

with the fourth invariant $I_4 = \mathbf{B} \cdot \mathbf{B}$.

Here, B_{ref} is a reference value of the magnetic flux density. Additionally, functions $g_i(I_1)$ for $i = \{0, 1, 2, 3, 4\}$ can be further approximated, as it is shown in Appendix A leading to:

$$\begin{aligned}g_0 &= \frac{3}{4} \alpha_0 \exp\left(\frac{3}{4} I_1\right) - \frac{1}{3} \left(\frac{1}{\mu_0} - \alpha_5\right) \\ g_i &= \frac{3(i+1)}{4} \alpha_i \exp\left(\frac{4(i+1)}{3} I_1\right) \quad \text{where } i = \{1, 2, 3, 4\}.\end{aligned}\tag{64}$$

The parameters α_i for $i = \{0, 1, 2, 3, 4, 5\}$ refer to the ferromagnetic structure due to the magnetization effect, see [16].

3.1.3. Magnetostrictive contribution. Magnetostriction is a constitutional characteristic of magnetic material related to electron spin or orbit orientations, their interactions, and molecular lattice geometry. The magnetostriction effect does not degrade in time or during usage. A magnetostrictive material does not present the magnetostriction effect when it is heated above its Curie temperature [82]. Curie temperature is defined as a transition point between ferromagnetic and paramagnetic behaviors. In magnetic materials, three types of magnetostriction mechanisms are determined to express the magnetostrictive feature of the magnetic material. These mechanisms are paramagnetic magnetostriction, spontaneous magnetostriction, and magnetostriction induced by

magnetic field [83]. Paramagnetism is a weak form of magnetism that is induced by an external field in the direction of the applied magnetic field. It will disappear when the magnetic field is removed. The spontaneous magnetization is followed by paramagnetism when a ferromagnetic material is cooled below its Curie temperature, so a transition from paramagnetism to ferromagnetism occurs, and magnetic moments cause a spontaneous magnetization effect [84]. In a magnetic material, the action of the external magnetic field [83] induces a magnetostriction effect by rotating and moving the internal magnetic domain walls.

We first employ two additional deformation-magnetization-dependent scalar-valued function (invariants) to represent magnetostrictive effect through:

$$I_5 = \mathbf{B} \cdot \boldsymbol{\varepsilon} \cdot \mathbf{B} \quad \text{and} \quad I_6 = \mathbf{B} \cdot \boldsymbol{\varepsilon}^2 \cdot \mathbf{B}. \quad (65)$$

The fifth and sixth invariants account for the magnetostrictive response as a function of the magnetic flux density \mathbf{B} and the mechanical strain $\boldsymbol{\varepsilon}$. The magnetostrictive density function is formulated as a function of (I_5, I_6) by:

$$W_{mos}(I_5, I_6, d) := \frac{1}{2}\alpha_5 I_5 + \frac{1}{2}\alpha_6 I_6. \quad (66)$$

Now we are able to define the magnetization vector \mathbf{M} as follows:

$$\begin{aligned} \mathbf{M}(\boldsymbol{\varepsilon}, \mathbf{B}; d) &:= -\frac{\partial W(\mathbf{B}, \boldsymbol{\varepsilon})}{\partial \mathbf{B}} = -\sum_i \frac{\partial W(\boldsymbol{\varepsilon}, \mathbf{B})}{\partial I_i} \frac{\partial I_i}{\partial \mathbf{B}} \\ &= -\frac{\partial W_{mag}(\boldsymbol{\varepsilon}, \mathbf{B})}{\partial I_4} \frac{\partial I_4}{\partial \mathbf{B}} - \sum_{i=5}^6 \frac{\partial W_{mos}(\boldsymbol{\varepsilon}, \mathbf{B})}{\partial I_i} \frac{\partial I_i}{\partial \mathbf{B}} \\ &= -\sum_{i=0}^4 \frac{g_i}{i+1} \partial_{I_4} \frac{I_4^{i+1}}{B_{\text{ref}}^{2i}} - \frac{1}{2} (\alpha_5 \mathbf{B} \cdot \boldsymbol{\varepsilon} - \alpha_6 \mathbf{B} \cdot \boldsymbol{\varepsilon}^2). \end{aligned} \quad (67)$$

For a detailed derivation, see Appendix A.

3.1.4. Elastic contribution. Since, the fracturing material behaves quite differently in bulk and shear parts of the domain, we employ a consistent split for the strain energy density function (68) into *tension* and *compression* counterparts, respectively. Following additive split for strain tensor in (17), the effective strain energy density ψ_e admits the additive decomposition

$$\psi_e(I_1, I_2) := \psi_e^{vol}(I_1) + \psi_e^{dev}(I_1, I_2), \quad (68)$$

with

$$\psi_e^{vol}(I_1) = \frac{K_n}{2} I_1^2 \quad \text{and} \quad \psi_e^{dev}(I_1, I_2) = \mu \left(\frac{I_1^2}{3} - I_2 \right), \quad \text{note } K_n, \mu > 0. \quad (69)$$

Here, $K_n = \lambda + \frac{2}{3}\mu$ is the bulk modulus which includes elastic Lamé's constant λ and the shear modulus μ . Additionally, I_1 and I_2 denote the invariants

$$I_1 = \text{tr}[\boldsymbol{\varepsilon}] \quad \text{and} \quad I_2 = \text{tr}[\boldsymbol{\varepsilon}^2]. \quad (70)$$

The isotropic strain energy density function given in (68) is additively decomposed into tension and compression contributions:

$$\psi_e(I_1, I_2) = \psi_e^+(I_1, I_2) + \psi_e^-(I_1), \quad (71)$$

where

$$\psi_e^+(I_1, I_2) = H^+[I_1]\psi_e^{vol}(I_1) + \psi_e^{dev}(I_1, I_2) \quad \text{and} \quad \psi_e^-(I_1) = (1 - H^+[I_1])\psi_e^{vol}(I_1). \quad (72)$$

Therein, $H^+[I_1(\boldsymbol{\varepsilon}^e)]$ is a *positive Heaviside function* which returns one if $I_1(\boldsymbol{\varepsilon}^e) > 0$ and zero if $I_1(\boldsymbol{\varepsilon}^e) \leq 0$. The total elastic contribution to the pseudo-energy density in (61) finally reads

$$W_{elas}(\boldsymbol{\varepsilon}, d) := g_e(d) [\psi_e^+(I_1, I_2)] + \psi_e^-(I_1), \quad (73)$$

where $g_e(d)$ is a *elastic degradation function*. Here, the standard monotonically decreasing quadrature degradation function, reads as $g_e(d) := (1 - \kappa)(1 - d)^2 + \kappa$. Here, κ is a very small parameter (to avoid numerical instabilities), and mathematically it is also depends on the discretization space, see [85].

We note that, the current resulting degraded stress tensor by the bulk energy is rely on the *vol/dev* decomposition. But, it is also possible to enhance (73), for the material which are sensitive to the shear fracture as it is investigated in rock-like materials, e.g. [86, 87]. So, to explore different characteristic behavior of fracture which is subjected to compression and shear modes for ferromagnetic materials, we could introduce different crack phase-field driving force. This subject is open for further investigation.

The Cauchy stress tensor is defined as a derivative of the free energy function with respect to the strain tensor as follows

$$\begin{aligned} \boldsymbol{\sigma}(\boldsymbol{\varepsilon}, \mathbf{B}, d) &:= \frac{\partial W}{\partial \boldsymbol{\varepsilon}} = \sum_i \frac{\partial W}{\partial I_i} \frac{\partial I_i}{\partial \boldsymbol{\varepsilon}} \\ &= \underbrace{g_e(d)\tilde{\boldsymbol{\sigma}}^+(\boldsymbol{\varepsilon}) + \tilde{\boldsymbol{\sigma}}^-(\boldsymbol{\varepsilon})}_{\text{elasticity term}} + \underbrace{\frac{1}{2} \sum_{i=0}^4 \frac{1}{i+1} \partial_{I_1} g_i \frac{I_4^{i+1}}{B_{\text{ref}}^{2i}} \mathbf{I}}_{\text{magnetization term}} \\ &\quad + \underbrace{\frac{1}{2} \alpha_5 \mathbf{B} \otimes \mathbf{B} + \frac{1}{2} \alpha_6 (\mathbf{B} \otimes \mathbf{B} \cdot \boldsymbol{\varepsilon} + \boldsymbol{\varepsilon} \cdot \mathbf{B} \otimes \mathbf{B})}_{\text{magnetostrictive term}}. \end{aligned} \quad (74)$$

with,

$$\tilde{\boldsymbol{\sigma}}^+(\boldsymbol{\varepsilon}) = K_n H^+(I_1)(\boldsymbol{\varepsilon} : \mathbf{I})\mathbf{I} + 2\mu \boldsymbol{\varepsilon}^{dev}, \quad \text{and} \quad \tilde{\boldsymbol{\sigma}}^-(\boldsymbol{\varepsilon}) = K_n (1 - H^+(I_1))(\boldsymbol{\varepsilon} : \mathbf{I})\mathbf{I}. \quad (75)$$

In addition to the Cauchy stress tensor, we have a stress tensor induced by the electromagnetic effects, denoted as $\boldsymbol{\tau}_m$ [88]. This electromagnetic-induced stress tensor is expressed by the Lorentz force, which furnishes an association between electromagnetism and the mechanics of the material. In accordance to [16, 88, 17], the second-order electromagnetic stress tensor defined as:

$$\begin{aligned} \boldsymbol{\tau}_m(\mathbf{B}; d) &= \underbrace{\frac{E_M}{\mu_0} \left(\mathbf{B} \otimes \mathbf{B} - \frac{1}{2} (\mathbf{B} \cdot \mathbf{B}) \mathbf{I} \right) + (\mathbf{M} \cdot \mathbf{B}) \mathbf{I} - \mathbf{B} \otimes \mathbf{M}}_{\text{magnetic response}} \\ &\quad + \underbrace{\epsilon_0 \left(\mathbf{E} \otimes \mathbf{E} - \frac{1}{2} (\mathbf{E} \cdot \mathbf{E}) \mathbf{I} + \mathbf{E} \times \mathbf{B} \otimes \dot{\mathbf{x}} \right)}_{\text{electric response}}. \end{aligned} \quad (76)$$

We note that in the case of polarization effect, the above equation, i.e., (76), should also include this effect, see [88] Chapter 15. Here, $E_M > 0$ is a constant material property which is known as the magnetostrictive viscosity constant [20]. Since, in the vacuum/air ($\mathbf{x} \in \Omega \setminus \mathcal{B}$) the magnetization effect disappears, thus results in $\mathbf{M} = \mathbf{0}$, in the electromagnetic stress (76). Additionally, since we only consider here for ferromagnetic material thus, we only take into account magnetic response in the quasi-static state, so the electric response in (76) is not considered. This assumption is acceptable for many materials which only represent the magnetic forces, e.g., iron; see for more detailed discussion [17, 16]. For further information related to the derivation of the stress expression, which contains the electromagnetically-dependent fields and parameters, you can refer to [12, 11, 13, 23].

Finally, the reduced second-order stress tensor (by removing the effect of electric response for the quasi-static state) is defined as

$$\begin{cases} \tau_m(\mathbf{B}; d) = \frac{E_M}{\mu_0} (\mathbf{B} \otimes \mathbf{B} - \frac{1}{2} (\mathbf{B} \cdot \mathbf{B}) \mathbf{I}) + (\mathbf{M} \cdot \mathbf{B}) \mathbf{I} - \mathbf{B} \otimes \mathbf{M} & \text{if } \mathbf{x} \in \mathcal{B} \\ \tau_m(\mathbf{B}; d) = \frac{E_M}{\mu_0} (\mathbf{B} \otimes \mathbf{B} - \frac{1}{2} (\mathbf{B} \cdot \mathbf{B}) \mathbf{I}) & \text{if } \mathbf{x} \in \Omega \setminus \mathcal{B} \end{cases}. \quad (77)$$

Therefore, the total stress tensor is given in the solid domain \mathcal{B} for a ferromagnetic material as:

$$\boldsymbol{\tau}(\boldsymbol{\varepsilon}, \mathbf{B}, d) = \boldsymbol{\sigma}(\boldsymbol{\varepsilon}, \mathbf{B}, d) + \boldsymbol{\tau}_m(\mathbf{B}; d). \quad (78)$$

By substituting the Cauchy stress tensor and the electromagnetic stress considering the magnetization effect, the total stress tensor follows

$$\begin{aligned} \boldsymbol{\tau}(\boldsymbol{\varepsilon}, \mathbf{B}, d) = & g_e(d) \tilde{\boldsymbol{\sigma}}^+(\boldsymbol{\varepsilon}) + \tilde{\boldsymbol{\sigma}}^-(\boldsymbol{\varepsilon}) + \frac{1}{2} \sum_{i=0}^4 \frac{1}{i+1} \partial_{I_1} g_i \frac{I_4^{i+1}}{B_{\text{ref}}^{2i}} \mathbf{I} \\ & + \left(E_M \mu_0^{-1} + \sum_{i=0}^4 \frac{g_i}{i+1} \partial_{I_4} \frac{I_4^{i+1}}{B_{\text{ref}}^{2i}} + \frac{1}{2} \alpha_5 \right) \mathbf{B} \otimes \mathbf{B} \\ & - \left(\frac{E_M}{2} \mu_0^{-1} + \sum_{i=0}^4 \frac{g_i}{i+1} \partial_{I_4} \frac{I_4^{i+1}}{B_{\text{ref}}^{2i}} \right) \mathbf{B} \cdot \mathbf{B} \mathbf{I} \\ & + \frac{1}{2} \alpha_5 (\mathbf{B} \otimes \mathbf{B} \cdot \boldsymbol{\varepsilon} - (\mathbf{B} \cdot \boldsymbol{\varepsilon} \cdot \mathbf{B}) \mathbf{I}) \\ & + \frac{1}{2} \alpha_6 (\mathbf{B} \otimes \mathbf{B} + \mathbf{B} \otimes \mathbf{B} \cdot \boldsymbol{\varepsilon}^2 - (\mathbf{B} \cdot \boldsymbol{\varepsilon}^2 \cdot \mathbf{B}) \mathbf{I} + (\mathbf{B} \otimes \mathbf{B} \cdot \boldsymbol{\varepsilon} + \boldsymbol{\varepsilon} \cdot \mathbf{B} \otimes \mathbf{B})). \end{aligned} \quad (79)$$

Additionally the magnetic flux \mathbf{H} can be specified

$$\mathbf{H}(\boldsymbol{\varepsilon}, \mathbf{B}; d) = \frac{1}{\mu_0} \mathbf{B} - 2 \sum_{i=0}^4 \frac{g_i}{i+1} \frac{\partial I_4^{i+1}}{\partial I_4} - \frac{1}{2} (\alpha_5 \mathbf{B} \cdot \boldsymbol{\varepsilon} + \alpha_6 \mathbf{B} \cdot \boldsymbol{\varepsilon}^2). \quad (80)$$

Remark 3.1. We note the traction force vector $\bar{\mathbf{t}} = \boldsymbol{\tau} \cdot \mathbf{n}$ is generally decomposed through the mechanic, electric, and magnetic fields' so-called generalized traction vector. If we

define $\bar{\mathbf{t}}$ as a mechanical traction force vector only only mechanical contribution $\tilde{\boldsymbol{\sigma}}$ exist, while the traction force vector for the electric and magnetic fields will be neglected, and set as zero at Neumann boundary conditions [89]. Additionally, the traction force due to the electric field is discussed in [90], which one can evaluate the electrostatic traction through the so-called Maxwell stress tensor. Also, regarding the magnetic force vector, the resultant magnetic force is divided into magnetic traction and body forces [91]. Let's define traction vector as the interaction between two adjacent surface elements. Traction magnetic force is computed based on potential magnetic force inside and outside of the magnetizable body. Thus, magnetic traction can be seen as the jumping value of a physical quantity between two sides of the surface [91]. So, the Neumann boundary conditions can be set for the magnetization jump between two adjacent magnetized surfaces. The traction force in magnetic separators is also investigated in [92]. Additionally, the electromagnetic traction due to electromagnetic stress tensor is described in [93]. They discussed whether the electromagnetic effects enter as a body force or as a surface stress, but not both. This is same as our case where we have only body force.

3.1.5. Fracture contribution. The fracture contribution of the pseudo-energy density given in (61) reads:

$$W_{frac}(d, \nabla d) := G_c \gamma_l(d, \nabla d), \quad (81)$$

where $G_c > 0$ is so-called a Griffith's energy release rate. In this study, we use a small time increment $\Delta t = t_{n+1} - t_n$ where t_n denotes the previous time step. This reduces the complexity of the problem. We further assume that:

$$\mu_0(d, t) \approx \mu_0(d, t_n), \quad \epsilon_0(d, t) \approx \epsilon_0(d, t_n), \quad (82)$$

$$\sigma_0(d, t) \approx \sigma_0(d, t_n), \quad \rho_0(d, t) \approx \rho_0(d, t_n).$$

This type of assumption has already been employed in hydraulic phase-field fracture. See, for instance, [94, 95], where the second-order anisotropic permeability tensor is computed of the previous time t_n . Finally, by taking the first variational derivative $\delta_d W$ of (61), the positive crack driving state function $\mathcal{D}(\mathbf{x}, t)$ follows

$$\mathcal{D} := \frac{2l_d}{G_c} \psi_e^+(I_1, I_2). \quad (83)$$

3.2. Variational formulations for the coupled multi-field problem

The variational formulations with respect to the four PDEs described in the previous sections for failure mechanics of ferromagnetic materials under the magnetostrictive effects are further discussed. The rate-dependent PDEs models, discussed in the previous section, are defined in a temporal domain $[t_n, t_{n+1}]$ with $\Delta t = t_{n+1} - t_n > 0$ holds. For the time-dependent problem in electromagnetic-induced fracture, we require initial conditions at $t = 0$ as:

$$\begin{aligned} \mathbf{u}^0 &= \mathbf{u}(\mathbf{x}, 0), & d^0 &= d(\mathbf{x}, 0), \\ \mathbf{E}^0 &= \mathbf{E}(\mathbf{x}, 0), & \mathbf{H}^0 &= \mathbf{H}(\mathbf{x}, 0), \\ \mathbf{D}^0 &= \mathbf{D}(\mathbf{x}, 0), & \mathbf{B}^0 &= \mathbf{B}(\mathbf{x}, 0), \end{aligned} \quad (84)$$

where \mathbf{H}^0 has to satisfy the divergence -free assumption

$$\nabla \cdot (\mu_0 \mathbf{H}^0(\mathbf{x})) = 0 \quad \text{in } \Omega \quad \text{and} \quad \mathbf{H}^0 \cdot \mathbf{N} = 0 \quad \text{on } \partial\Omega. \quad (85)$$

3.2.1. Electromagnetic contribution. The magnetostatic response is a special case of the electromagnetic problem which is obtained when the electric field $\mathbf{E}(\mathbf{x}, t)$ does not change by time, and thus $\partial \mathbf{D} / \partial t = 0$. This results in

$$\frac{\partial \mathbf{D}(\mathbf{x}, t)}{\partial t} = \epsilon_0 \frac{\partial \mathbf{E}(\mathbf{x}, t)}{\partial t} = \mathbf{0}. \quad (86)$$

The variation of the electric displacement in time is 0, and thus we can assume that permittivity is zero, i.e., $\epsilon_0 = 0$. The time-discretized variational formulation of the evolution equation of the magnetic vector potential $\mathbf{A}(\mathbf{x}, t)$ in (42) is derived by multiplying it with the test function $\delta \mathbf{A}$ and then applying integrating by part

$$\begin{aligned} \mathcal{E}_{\mathbf{A}}(\mathbf{u}, \delta \mathbf{A}) &= \Delta t \int_{\Omega} \frac{1}{\mu_0(d)} \nabla \mathbf{A} : \nabla(\delta \mathbf{A}) \, d\mathbf{x} + \int_{\Omega} \sigma_0(d) [(\mathbf{A} - \mathbf{A}^n) + \Delta t \nabla \Phi] \cdot \delta \mathbf{A} \, d\mathbf{x} \\ &\quad - \Delta t \int_{\Omega} \mathbf{J}_s(t) \cdot \delta \mathbf{A} \, d\mathbf{x} = 0 \quad \forall \delta \mathbf{A} \in \mathcal{S}_0^v(\text{curl}; \Omega), \end{aligned} \quad (87)$$

where (42) is imposed.

3.2.2. Elastic contribution. The variational formulations of the strong formulation of the Euler-Lagrange equations with respect to the $\mathbf{u}(\mathbf{x}, t)$ in Formulation 2.a reads:

$$\mathcal{E}_{\varepsilon}(\mathbf{u}, \delta \mathbf{u}) = \int_{\mathcal{B}} [\boldsymbol{\tau} : \delta \boldsymbol{\varepsilon} - \bar{\mathbf{b}} \cdot \delta \mathbf{u}] \, d\mathbf{x} - \int_{\partial_N^u \mathcal{B}} \bar{\mathbf{t}} \cdot \delta \mathbf{u} \, ds = 0 \quad \forall \delta \mathbf{u} \in \mathcal{W}_0^u(\text{div}; \mathcal{B}). \quad (88)$$

We note that $\mathcal{E}_{\varepsilon}(\mathbf{u}, \delta \mathbf{u})$ unlike the magnetic vector potential given in (87), lives in \mathcal{B} (and not Ω). Since $\boldsymbol{\tau}$ is a function of \mathbf{B} (and not \mathbf{A}), the local constitutive equation $\mathbf{B} = \nabla \times \mathbf{A}$ has to be imposed after solving magnetic vector potential from (87).

3.2.3. Fracture contribution. The variational formulation of the strong formulation of fracture with respect to the crack phase-field $d(\mathbf{x}, t)$ in Formulation 2.a reads:

$$\begin{aligned} \mathcal{E}_d(\mathbf{u}, \delta d) &= (1 - \kappa) \Delta t \int_{\mathcal{B}} (d - 1) \mathcal{H} \cdot \delta d \, d\mathbf{x} + \int_{\mathcal{B}} [\Delta t d \cdot \delta d + \eta_d (d - d^n) \cdot \delta d] \, d\mathbf{x} \\ &\quad + \int_{\mathcal{B}} [l_d^2 \Delta t \nabla d \cdot \nabla(\delta d)] \, d\mathbf{x} = 0 \quad \forall \delta d \in \mathcal{W}_0^d(\text{div}; \mathcal{B}). \end{aligned} \quad (89)$$

As in the weak form $\mathcal{E}_{\varepsilon}(\mathbf{u}, \delta \mathbf{u})$, the crack phase-field equation lives in \mathcal{B} .

Thus, by means of (87), (88), and (89), the fully coupled variational multi-field problem to describing magnetostrictive induced fractures in ferromagnetic material is formulated in the compact form as:

$$\begin{aligned} \mathcal{E}_{\mathbf{u}}(\mathbf{u}, \delta \mathbf{u}) &= \mathcal{E}_{\varepsilon}(\mathbf{u}, \delta \mathbf{u}) + \mathcal{E}_{\mathbf{A}}(\mathbf{u}, \delta \mathbf{A}) + \mathcal{E}_d(\mathbf{u}, \delta d) = 0 \\ &\quad \forall (\delta \mathbf{u}, \delta \mathbf{A}, \delta d) \in \left(\mathcal{W}_0^u(\text{div}; \mathcal{B}), \mathcal{S}_0^v(\text{curl}; \Omega), \mathcal{W}_0^d(\text{div}; \mathcal{B}) \right). \end{aligned} \quad (90)$$

In order to solve the magnetostrictive induced fracture system (90), we first solve the first two equations monolithically (simultaneously obtain (\mathbf{u}, \mathbf{A})). Then, a staggered approach is employed to obtain the phase-field fracture d . To that end, we fix alternately (\mathbf{u}, \mathbf{A}) and estimate d and vice versa. The procedure is continued until convergence (using a given TOL_{Stag}). The alternate minimization scheme applied to the (90) is summarized in Algorithm 1.

Algorithm 1 *The staggered iterative solution process for (90) at a fixed time-step n .*

Input: loading data $\bar{\mathbf{t}}_n$ on $\partial_N^u \mathcal{B}$ and $\mathbf{J}_s(t)$ on wires

solution $(\mathbf{u}^{n-1}, \mathbf{A}^{n-1}, d^{n-1})$ from step $n - 1$.

Initialization, $k = 1$:

- set $(\mathbf{u}^0, \mathbf{A}^0, d^0) := (\mathbf{u}^{n-1}, \mathbf{A}^{n-1}, d^{n-1})$.

Staggered iteration between (\mathbf{u}, \mathbf{A}) and d :

- solve following system of equations in a monolithic manner by given d^{k-1} ,

$$\left\{ \begin{array}{l} \Delta t \int_{\Omega} \frac{1}{\mu_0(d)} \nabla \mathbf{A} : \nabla (\delta \mathbf{A}) \, d\mathbf{x} + \int_{\Omega} \sigma_0(d) [(\mathbf{A} - \mathbf{A}^n) + \Delta t \nabla \Phi] \cdot \delta \mathbf{A} \, d\mathbf{x} - \Delta t \int_{\Omega} \mathbf{J}_s(t) \cdot \delta \mathbf{A} \, d\mathbf{x} = 0, \\ \int_{\mathcal{B}} [\boldsymbol{\tau}(\boldsymbol{\varepsilon}, \mathbf{B}, d) : \delta \boldsymbol{\varepsilon} - \bar{\mathbf{b}} \cdot \delta \mathbf{u}] \, d\mathbf{x} - \int_{\partial_N^u \mathcal{B}} \bar{\mathbf{t}} \cdot \delta \mathbf{u} \, ds = 0 \quad \text{with } \mathbf{B} = \nabla \times \mathbf{A}, \end{array} \right.$$

for (\mathbf{u}, \mathbf{A}) , set $(\mathbf{u}, \mathbf{A}) =: (\mathbf{u}^k, \mathbf{A}^k)$,

- given $(\mathbf{u}^k, \mathbf{B}^k)$, solve

$$(1 - \kappa) \Delta t \int_{\mathcal{B}} (d - 1) \mathcal{H} \cdot \delta d \, d\mathbf{x} + \int_{\mathcal{B}} [\Delta t d \cdot \delta d + \eta_d (d - d^n) \cdot \delta d] \, d\mathbf{x} + \int_{\mathcal{B}} [l_d^2 \Delta t \nabla d \cdot \nabla (\delta d)] \, d\mathbf{x} = 0$$

for d , set $d =: d^k$,

- for the obtained pair $(\mathbf{u}^k, \mathbf{A}^k, d^k)$, check staggered residual by

$$\text{Res}_{\text{Stag}}^k : |\mathcal{E}_{\boldsymbol{\varepsilon}}(\boldsymbol{\mathfrak{U}}^k; \delta \mathbf{u})| + |\mathcal{E}_{\mathbf{A}}(\boldsymbol{\mathfrak{U}}^k; \delta \mathbf{A})| \leq \text{TOL}_{\text{Stag}}$$

- if fulfilled, set $\boldsymbol{\mathfrak{U}}^k = (\mathbf{u}^k, \mathbf{A}^k, d^k) =: (\mathbf{u}^n, \mathbf{A}^n, d^n) = \boldsymbol{\mathfrak{U}}^n$ then stop;

else $k + 1 \rightarrow k$.

Output: solution $(\mathbf{u}^n, \mathbf{A}^n, d^n)$ at n^{th} time-step.

Remark 3.2. *Since the permeability of the ferromagnetic material is computed as a function of the crack phase-field with a degrading function, the magnetic vector potential \mathbf{A} , the magnetic field \mathbf{B} and the magnetic flux \mathbf{H} are implicitly determined as a function of the crack phase-field. Therefore, when a crack starts to propagate in the material, the degradation function actively represents its degrading effect on the magnetic response of the material. Then, the magnetic vector potential \mathbf{A} , the magnetic field \mathbf{B} and the magnetic flux \mathbf{H} decrease along the crack paths.*

3.3. Space finite element discretization

In this section, we provide spatial discretizations of the variational forms given in Algorithm 1. This results in a discretized multi-field problem to be solved for three-field unknowns represented by $(\mathbf{u}, \mathbf{A}, d)$. In the case of the magnetostatic problem, one can use either Nédélec elements or alternatively $H^1(\Omega)$ conforming elements with continuous piecewise polynomials, see [96]. We use a Galerkin finite element method to discretize the equations, employing second order isoparametric curl-conforming triangular element P_2 for the ansatz and test spaces of all primary fields see [97, 98, 99, 100, 101, 102]. The continuous solid domains \mathcal{B} , and the vacuum domain Ω are approximated by \mathcal{B}_h , and Ω_h such that $\mathcal{B} \approx \mathcal{B}_h$, and $\Omega \approx \Omega_h$. The approximated domains \mathcal{B}_h , and Ω_h are decomposed with non-overlapping linear triangular finite element $\mathcal{B}_e \subset \mathcal{B}_h$ such that

$$\mathcal{B} \approx \mathcal{B}_h = \bigcup_e^{n_e} \mathcal{B}_e \quad \text{and} \quad \Omega \approx \Omega_h = \bigcup_e^{n_e} \Omega_e. \quad (91)$$

The unknown fields $(\mathbf{u}, \mathbf{A}, d)$ are approximated by

$$\mathbf{u}_h = \mathbf{N}_u \hat{\mathbf{u}}, \quad d_h = \mathbf{N}_d \hat{\mathbf{d}}, \quad \mathbf{A}_h = \mathbf{N}_A \hat{\mathbf{A}}. \quad (92)$$

with a set of nodal solution values $(\hat{\mathbf{u}}, \hat{\mathbf{d}}, \hat{\mathbf{A}})$. Their derivatives are given by

$$\boldsymbol{\varepsilon}(\mathbf{u}_h) = \mathbf{B}_u \hat{\mathbf{u}}, \quad \nabla d_h = \mathbf{B}_d \hat{\mathbf{d}}, \quad \nabla \mathbf{A}_h = \mathbf{B}_A \hat{\mathbf{A}}, \quad (93)$$

which represent constitutive state variables $(\boldsymbol{\varepsilon}_{\mathbf{u}_h}, \nabla d_h, \nabla \mathbf{A}_h)$. Here, \mathbf{B}_u , \mathbf{B}_d , \mathbf{B}_A are the matrix representation of the shape function's derivatives, corresponding to the global deformation, crack phase-field, and the magnetic vector potential, respectively. Additionally, the magnetic flux densities (which is enter to deformation equation) are approximated by the curl operator as:

$$\mathbf{B}(\mathbf{A}_h) = \nabla \times \mathbf{A}_h = \boldsymbol{\Pi} \hat{\mathbf{A}}. \quad (94)$$

Here, $\boldsymbol{\Pi}$ is the matrix representation of the shape function's derivative, see [16] (Section 3.2), and [103] for a detailed discussion. For each primary field, the set of discretized weak forms which is based on the *residual* force vector denoted by \mathbf{R}_\bullet has to be determined. First, the mechanical weak form leads to

$$\mathbf{R}_u(\mathbf{u}, d, \mathbf{A}) = \sum_e \int_{\mathcal{B}_e} [\mathbf{B}_u^T \boldsymbol{\tau}(\boldsymbol{\varepsilon}_h, \mathbf{B}_h, d_h) - \bar{\mathbf{b}} \cdot \mathbf{N}_u] \, d\mathbf{x} - \int_{\partial \mathcal{B}_N} \bar{\mathbf{t}} \cdot \mathbf{N}_u \, ds = \mathbf{0}, \quad (95)$$

next, for the magnetic vector potential yields,

$$\begin{aligned} \mathbf{R}_A(\mathbf{u}, d, \mathbf{A}) = \sum_e \int_{\Omega_e} \left[\frac{\Delta t}{\mu_0(d)} \mathbf{B}_A^T \nabla \mathbf{A} + \sigma_0(d) [(\mathbf{A} - \mathbf{A}^n) + \Delta t \nabla \Phi] \cdot \mathbf{N}_A \right. \\ \left. - \Delta t \mathbf{J}_s(t) \cdot \mathbf{N}_A \right] \, d\mathbf{x} = \mathbf{0}, \end{aligned} \quad (96)$$

and lastly the crack phase-field follows as:

$$\begin{aligned} \mathbf{R}_d(\mathbf{u}, d, \mathbf{A}) = \sum_e \int_{\mathcal{B}_e} \left[\left((1 - \kappa)(d_h - 1) \mathcal{H} + d + \frac{\eta_d}{\Delta t} (d_h - d_h^n) \right) \cdot \mathbf{N}_d \right. \\ \left. + l_d^2 \mathbf{B}_d^T \cdot \nabla d_h \right] \, d\mathbf{x} = \mathbf{0}. \end{aligned} \quad (97)$$

4. Numerical examples

In this section, the capability of the proposed framework in predicting the magneto-restrictively-induced cracking in the ferromagnetic materials is approved by demonstrating the numerical examples. At first, the evolution of the magnetic vector potential and the magnetic field in a ferromagnetic material is investigated. Then, cracking in the ferromagnetic materials is investigated by adopting the magneto-mechanical model coupled with the phase-field approach. The boundary-value problem of the first example is related to a domain that includes copper wires and an iron beam that are surrounded by vacuum. In the remaining examples, the domain of the boundary-value problems contains predefined notches and copper wires where a constant electric current source is enforced. These representative numerical examples are solved by developing a finite element software based on the FEniCS software library, see [104, 105]. The material parameters used in the numerical examples are listed in Table 1. For the staggered approach, see Algorithm 1, we set $\text{TOL}_{\text{stag}} = 10^{-4}$. We also note that the second term of anisotropic material constants in (58) is assumed for quasi-impermeable crack faces, hence we set $(\mu_0^f, \epsilon_0^f, \sigma_0^f, \rho_0^f)$ identical to vacuum counterparts.

Table 1: Material parameters used in the numerical examples based on [88]

No.	Parameter	Name	Example 1-2	Example 3	Unit
1.	E	Young's modulus	160	16	GPa
2.	ν	Poisson's ratio	0.33	0.2	–
3.	$\mu_{0,\Omega}$	Permeability of vacuum	$4\pi \times 10^{-7}$	—	H/mm
4.	$\mu_{0,\mathcal{W}}$	Permeability of wires	1.26×10^2	1.26×10^3	H/mm
5.	$\mu_{0,\mathcal{B}}$	Permeability in solid	1000	10^7	H/mm
6.	σ_0	Electromagnetic conductivity	1	1	S/mm
7.	B_{ref}	The magnetic flux density	2×10^6	2×10^6	T
8.	$(\alpha_0, \dots, \alpha_3)$	Magnetisation constants	2×10^{-6}	2×10^{-6}	–
9.	(α_4, α_5)	Magnetostrictive constants	(2.5, 7.75)	(2.5, 7.75)	–
10.	E_M	Magnetostrictive viscosity	10^{-9}	10^{-9}	–
11.	ζ	Permeability transition exponent	50	50	–
12.	η_d	damage viscosity	1×10^{-6}	1×10^{-6}	N/(mm ²)s
13.	$l_d = 2h_e$	fracture regularization parameter	2.196	2.196	–
14.	κ	Stabilization parameter	10^{-8}	10^{-8}	–
15.	G_c	Griffith's energy release rate	0.0027	0.0027	–
16.	(m, c_1, c_2)	degradation parameters	(2, 0.1, 0.9)	(2, 0.1, 0.9)	–

4.1. Example 1: Magnetostatic problem for transient magnetic vector potential

The first insight into the performance of the variational form of Maxwell's equations in a finite element context are gained by a two-dimensional transient magnetostatic problem in a domain composed of copper wires and an iron cylinder that are surrounded by a vacuum. The geometrical configuration of the 2D test problem and its finite element model are depicted in Figure 6, in which the subdomains for the iron cylinder, the copper wires, and the surrounding vacuum with the radius of $r_v = 5$ mm are clearly visible.

The inner radius of the cylinder is $r_1 = 1$ mm and its thickness is $n = 0.2$ mm. The domain contains ten copper wires with a radius of $r_w = 0.1$ mm. The discretization of the domain is performed with 64652 triangular elements with the minimum element size of $h_{\min} \approx 0.04$ mm.

The wires are assumed to carry the electric current, which is varied linearly with time. The electromagnetic waves are neglected, since the problem is supposed to be magnetostatics. To examine this problem, the Poisson-type equation (37) is solved. The specific current $\mathbf{J}_s(t)$ along the z -direction is given by

$$\text{exterior wires: } \mathbf{J}_s(t, z) = -t \text{ A/mm}^2, \quad \text{interior wires: } \mathbf{J}_s(t, z) = t \text{ A/mm}^2,$$

for the interior set of the winding copper wires. The results are obtained in terms of the magnetic vector potential in z -direction, $A_z(\mathbf{x}, t)$, for the different time steps, and the magnetic flux density $\mathbf{B}(\mathbf{x}, t)$ for the last time step. These results are shown in Figure 7 and Figure 8, respectively.

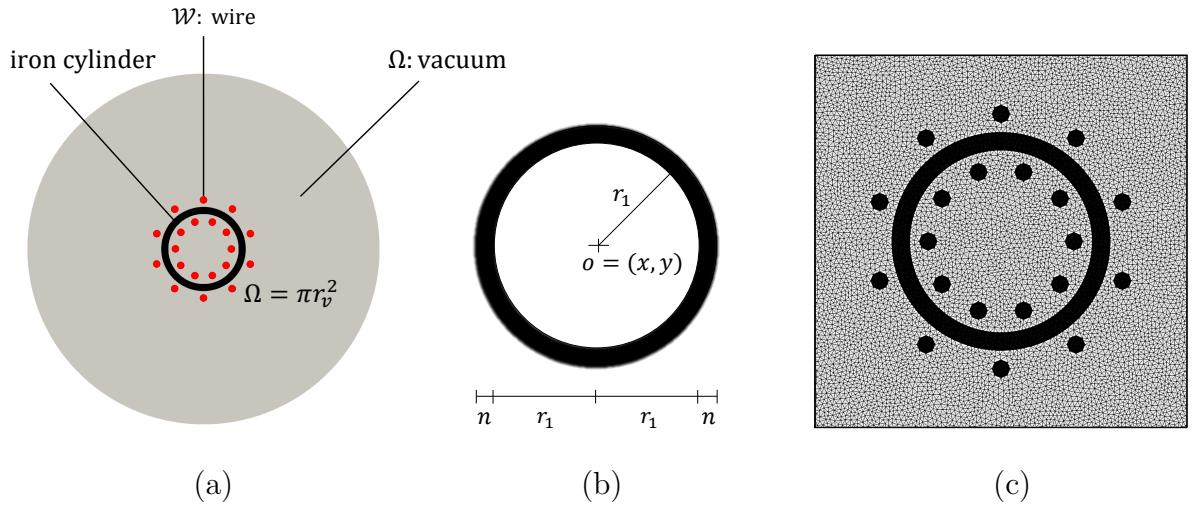


Figure 6: Example 1. The representation of (a) whole domain of the magnetostatic problem including copper wires winding around the iron cylinder and vacuum, (b) geometry and dimensions of iron cylinder, and (c) finite element mesh generated for the test problem. The subdomains for the iron cylinder and copper wires are clearly demonstrated.

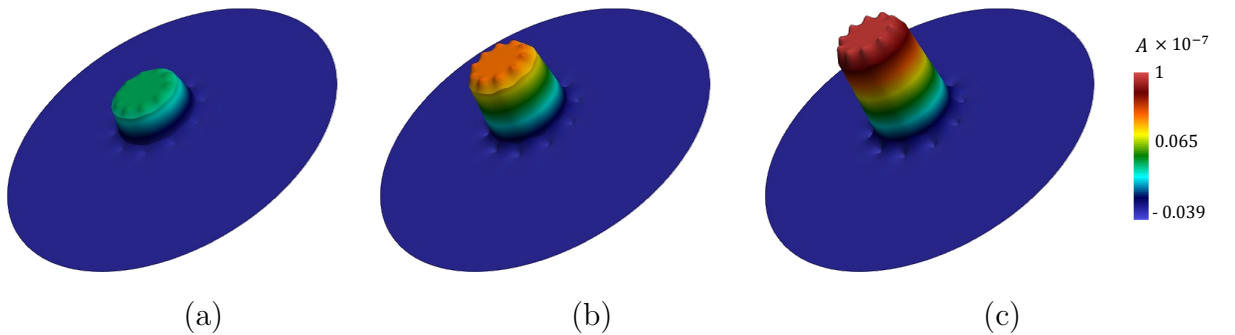


Figure 7: Example 1. The representation of the z -component of the magnetic vector potential A_z at (a) $t = 40$ s (b) $t = 80$ s (c) $t = 120$ s.

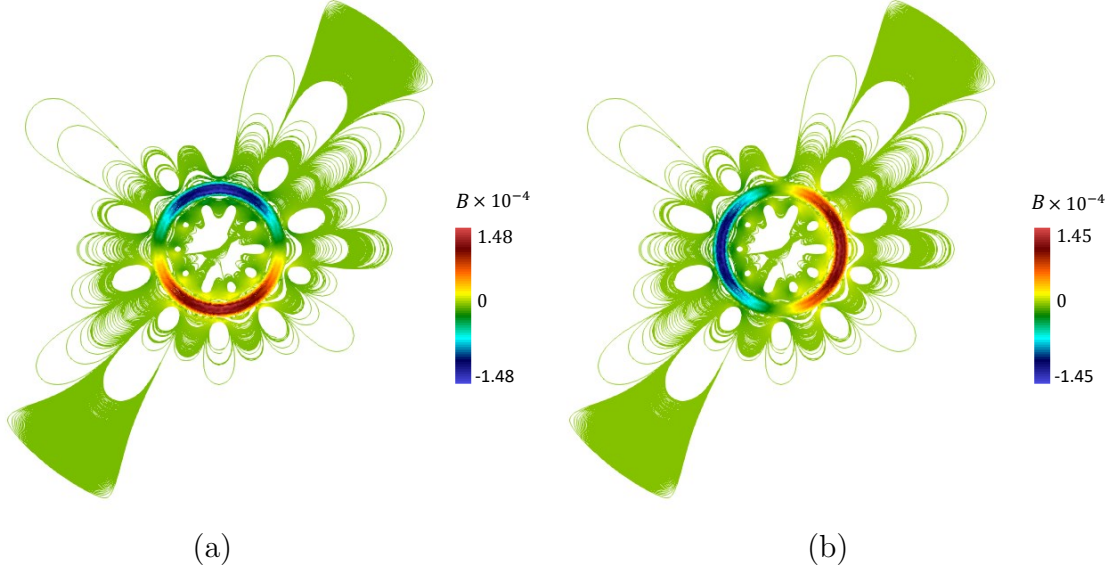


Figure 8: Example 1. The representation of (a) the x - and (b) y - components of the magnetic field field \mathbf{B} at $t = 120$ s

4.2. Example 2: Magneto-mechanically induced cracking in an iron beam surrounded by vacuum

The second example investigates the magnetostrictive-induced cracking in a ferromagnetic notched beam. This problem is solved by coupling the Poisson-type transient magnetic equation with the phase-field model. The domain of the boundary value problem consists of vacuum, two copper wires, and the single notched simply-supported iron beam. The electric current flows through the top and the bottom wires. The geometrical configuration and finite element model of the boundary value problem are displayed in Figure 9, respectively. The whole domain is composed of vacuum with the radius of $r_v = 8$ mm, two copper wires with the radius of $r_w = 0.5$ mm, and the notched iron beam with $n = 0.8$ mm and $m = 3.6$ mm located at the middle of the vacuum with the dimension of $A = 4$ mm and $B = 2$ mm hence $\mathcal{B} = (0, 4) \times (0, 2)$ mm². The whole domain is discretized with 28325 triangular elements. As the domain is divided into three subdomains, and the crack phase-field equation is only solved in the iron beam subdomain, the discretization is refined in that region. In this case, the minimum element size is $h_{\min} \approx 0.005$ mm and the maximum element size is $h_{\max} \approx 1.098$ mm, see Figure 9(c).

The wires located on the top and bottom of the iron beam contain the electric current. The specific current $\mathbf{J}_s(t)$ along the z -direction is given in the form of a linear equation which varies in time as wire.

$$\text{top wire: } \mathbf{J}_s(t, z) = 2.5t \text{ A/mm}^2, \quad \text{bottom wire: } \mathbf{J}_s(t, z) = -1.5t \text{ A/mm}^2.$$

At first, the evolution of magnetic vector potential $A_z(\mathbf{x}, t)$ and magnetic field $\mathbf{B}(\mathbf{x}, t)$ are calculated through Maxwell's equations in the whole domain. The stress response regarding the magnetostrictive effects is determined in the iron beam. The electric current flow in the wires generates magnetization in the notched iron beam that forces it to deform. The deformation causes stress development around the notch. Therefore, cracking starts to initiate when the maximum principal stress exceeds the critical value. The crack

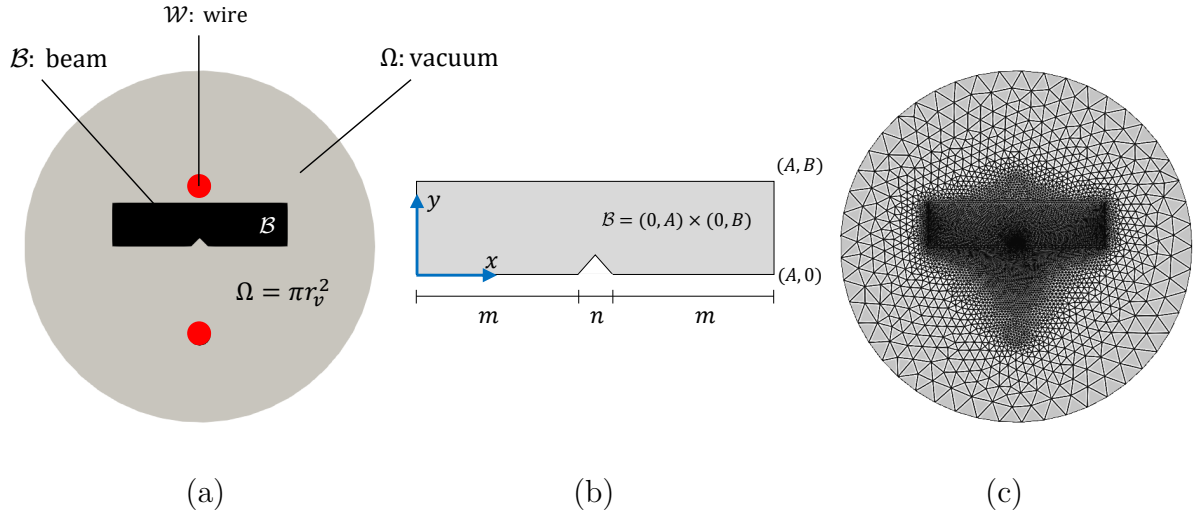


Figure 9: Example 2. The representation of geometries and dimensions of (a) whole domain, (b) iron beam, and (c) finite element model of BVP. The subdomains are clearly invisible.

initiation and propagation in the beam at different time steps are demonstrated in Figure 10. The magnetic vector potential $A_z(\mathbf{x}, t)$ and the magnetic field $\mathbf{B}(\mathbf{x}, t)$ at the last time step $t = 0.68$ s are exhibited in Figure 11.

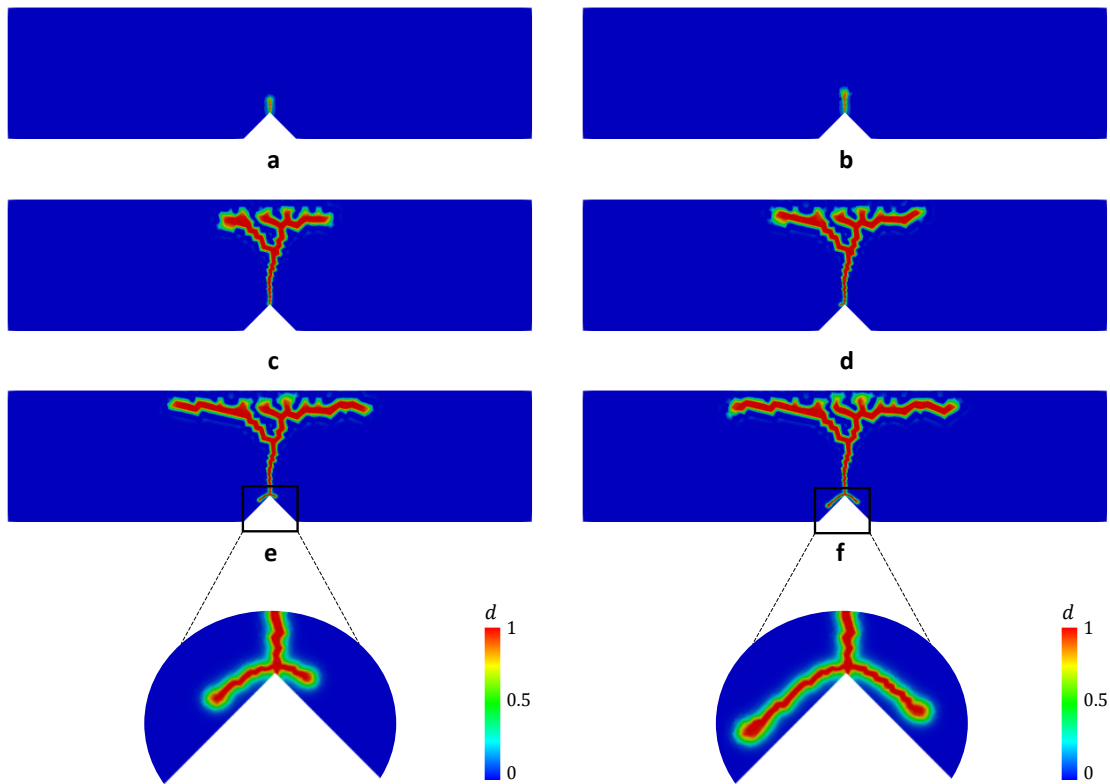


Figure 10: Example 2. The representation of the crack initiation and propagation in the iron beam under coupling electromagneto-mechanical effects at (a) $t = 0.43$ s, (b) $t = 0.45$ s, (c) $t = 0.56$ s, (d) $t = 0.59$ s, (e) $t = 0.64$ s and (f) $t = 0.68$ s.

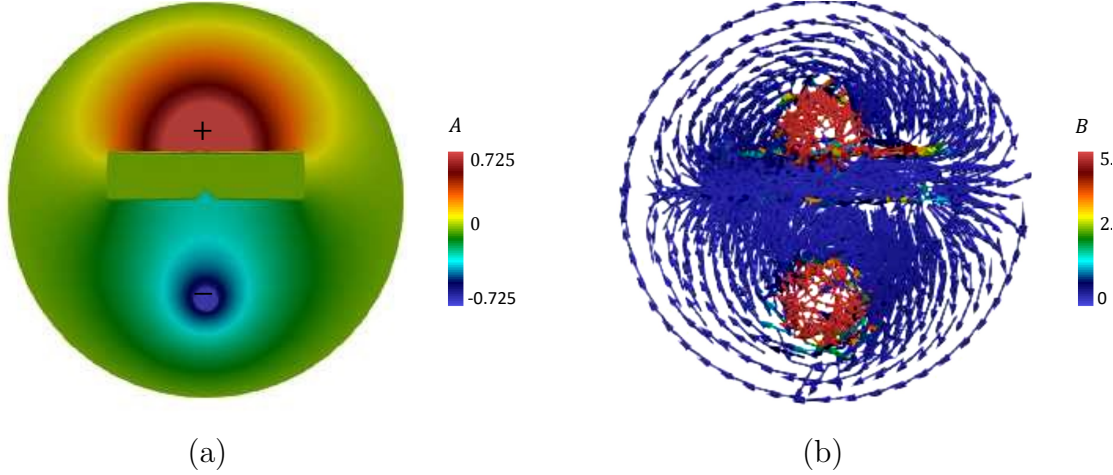


Figure 11: Example 2. The representation of (a) the magnetic vector potential A_z , and (b) the magnitude of the magnetic field \mathbf{B} at $t = 0.68$ s (final failure state).

4.3. Example 3: Magneto-mechanically induced cracking in a ferromagnetic material containing predefined notches and wires

This example comprises four sub-examples in which the magneto-mechanically driven fracture in a ferromagnetic material is examined. In the first two examples, the electric current is enforced through the notches, and in the last two examples, the electric current flows through the copper wires. The cracking response of the ferromagnetic material is examined by solving the coupled magneto-mechanically driven crack phase-field problem. The following sub-examples investigate a square plate of ferromagnetic material. The geometrical configuration of the first two examples with the predefined notches is shown in Figure 12. We set $A = 40$ mm thus $\mathcal{B} = (0, 80)^2$ mm². The discretization of the domain is performed with 51200 triangular elements with an element size of $h \approx 0.707$ mm. In the last two sub-examples, the square plates contain copper wires with the radius of $r_w = 0.3$ mm, see Figure 13. The third sub-example with four copper wires is discretized with 31132 triangular elements. In the domain, the uniform element size is $h \approx 1.02$ mm. The fourth sub-example with five copper wires is discretized with 30984 triangular elements by the uniform element size as $h \approx 1.02$ mm. In these BVPs, all displacements are fixed in both directions, and the electric vector potential is set to zero at the boundaries $\partial_D \mathcal{B}$. The notches and copper wires carry the constant electric source current of $\bar{J} = 0.03$ A/mm².

4.3.1. Sub-example 1: Transversely wired plate with three winding wires.

In this example, the domain contains three predefined notches \mathcal{C}_1 , \mathcal{C}_2 and \mathcal{C}_3 of length $n = 8$. The notch \mathcal{C}_1 is located horizontally in the center of the domain. The other vertical notches (\mathcal{C}_2 and \mathcal{C}_3) are located with distances of $m = 20$ mm from the right and left boundaries, see Figure 12(a). The results in terms of the crack phase-field, the magnetic vector potential A_z , and von Mises stress are exhibited in Figure 14. Moreover, the magnetic field \mathbf{B} developed in the plate is shown in Figure 18(a). The variation of the magnetic vector potential average value with respect to time it includes the effect of damage is represented in Figure 20.a.

4.3.2. Sub-example 2: Transversely wired plate with nine winding wires.

In this example, the square plate considered in the BVP contains nine predefined notches \mathcal{C}_i with $i = 1, 2, 3, \dots, 9$. The dimensions of the notches are the same as the previous sub-

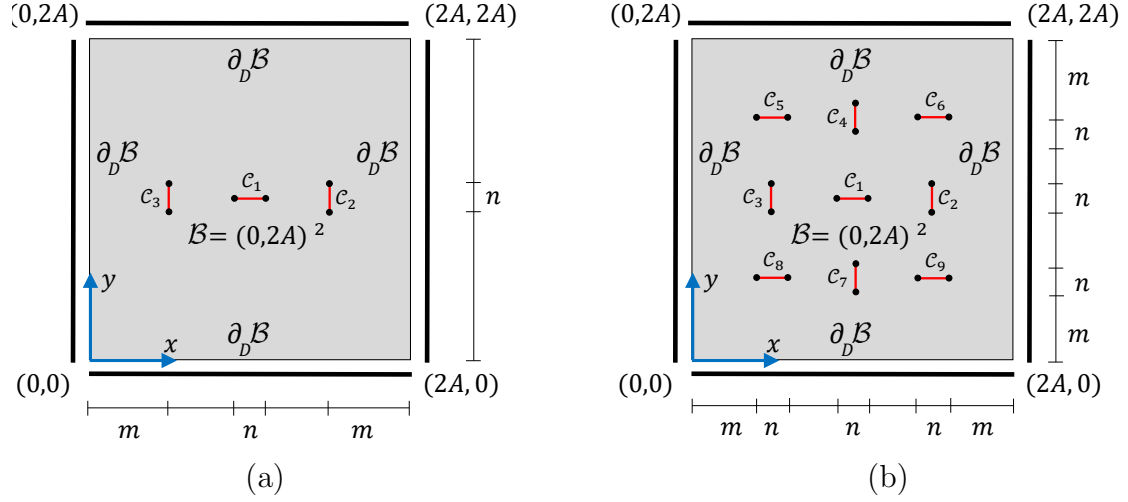


Figure 12: Transversely wired plates. The representation of geometry, the corresponding dimensions and the boundary conditions of the square plate contains (a) three predefined notches (Example 3.1), and (b) nine predefined notches (Example 3.2)

example, see Figure 12(b). The results in terms of the crack phase-field, magnetic vector potential, and von Mises stress are presented in Figure 15 at different time steps. The magnetic field arising in the plate under the constant electric current source is shown at the last time step in Figure 18.b. The average value of the magnetic vector potential over time in the square plate regarding the cracking effect is depicted in Figure 20(b).

In both sub-examples, it is observed that cracks start to evolve in the square plate when a constant electric current is enforced in the predefined notches. As the crack propagates over time, the electric vector potential increases along the crack. However, its value decreases when it does not reach the cracking state. The evolution of the average value of the magnetic vector potential over time confirms that when the plate is completely damaged, the value decreases. The comparison of the results indicates that the average value of the magnetic vector potential in the plate with nine notches reaches its maximum value earlier than in the plate with three notches.

4.3.3. Sub-example 3: Longitudinally wired plate with four winding wires.

In the third case, the square plate contains four copper wires, \mathcal{C}_i with $i = 1, 2, 3, 4$. The radius of the wires is $r_{\text{wire}} = 3$ mm. The dimensions of the plate are the same as the previous sub-examples, see Figure 12(a). The wires are placed of a distance of $m = 20$ mm from the edge of the plate. The crack initiation and propagation, the evolution of the magnetic vector potential, and the von Mises stress for the different time steps are presented in Figure 15. The magnetic field under the constant electric current is presented in Figure 18(a) for the last time step. The average value of the magnetic vector potential over time in the square plate regarding the cracking effect is provided in Figure 21.a.

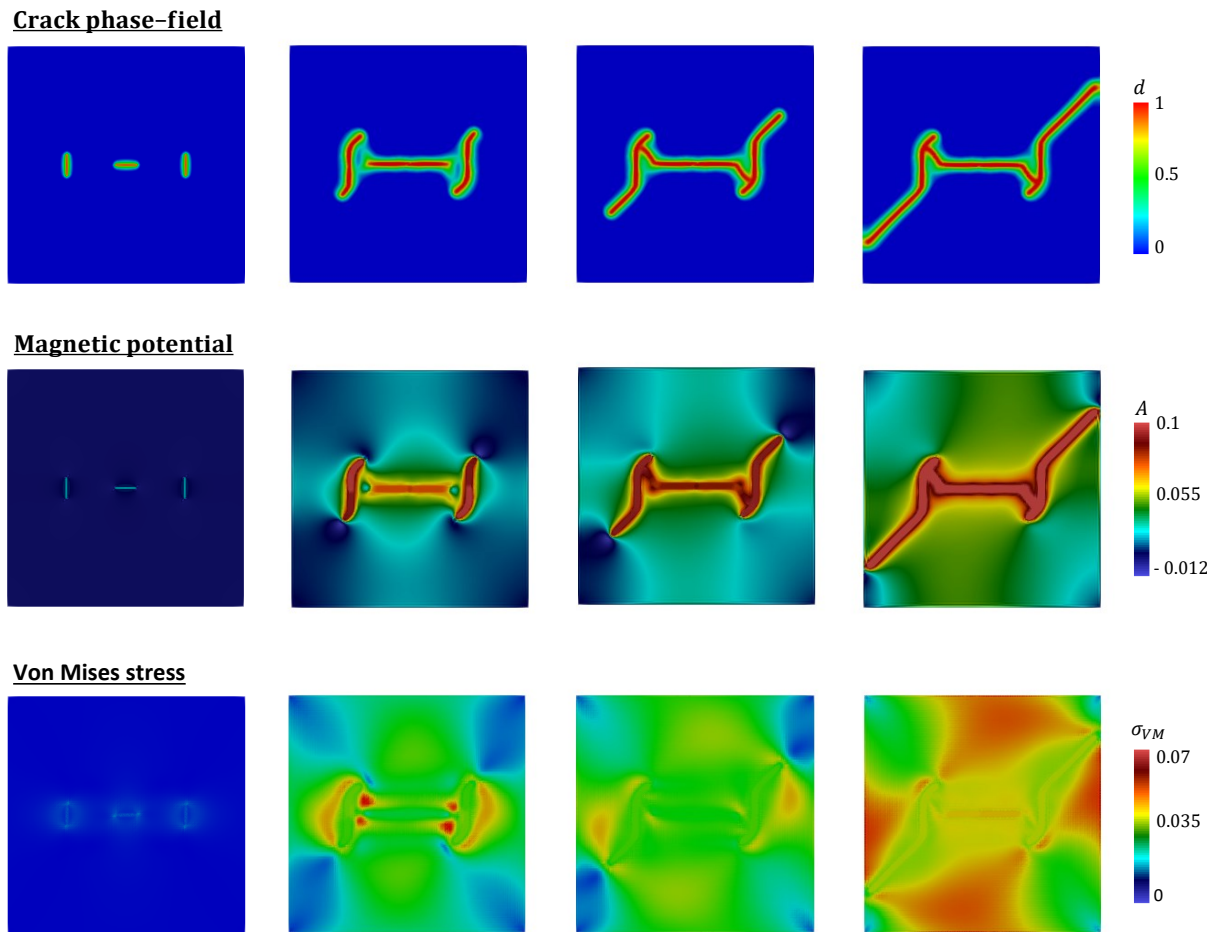


Figure 14: Example 3.1. Transversely wired plate with three winding wires. Reference results of the magnetostrictively induced crack driven by constant electric current source induction along the predefined notches. Evolution of the crack phase-field, magnetic vector potential and von Mises stress at different time steps.

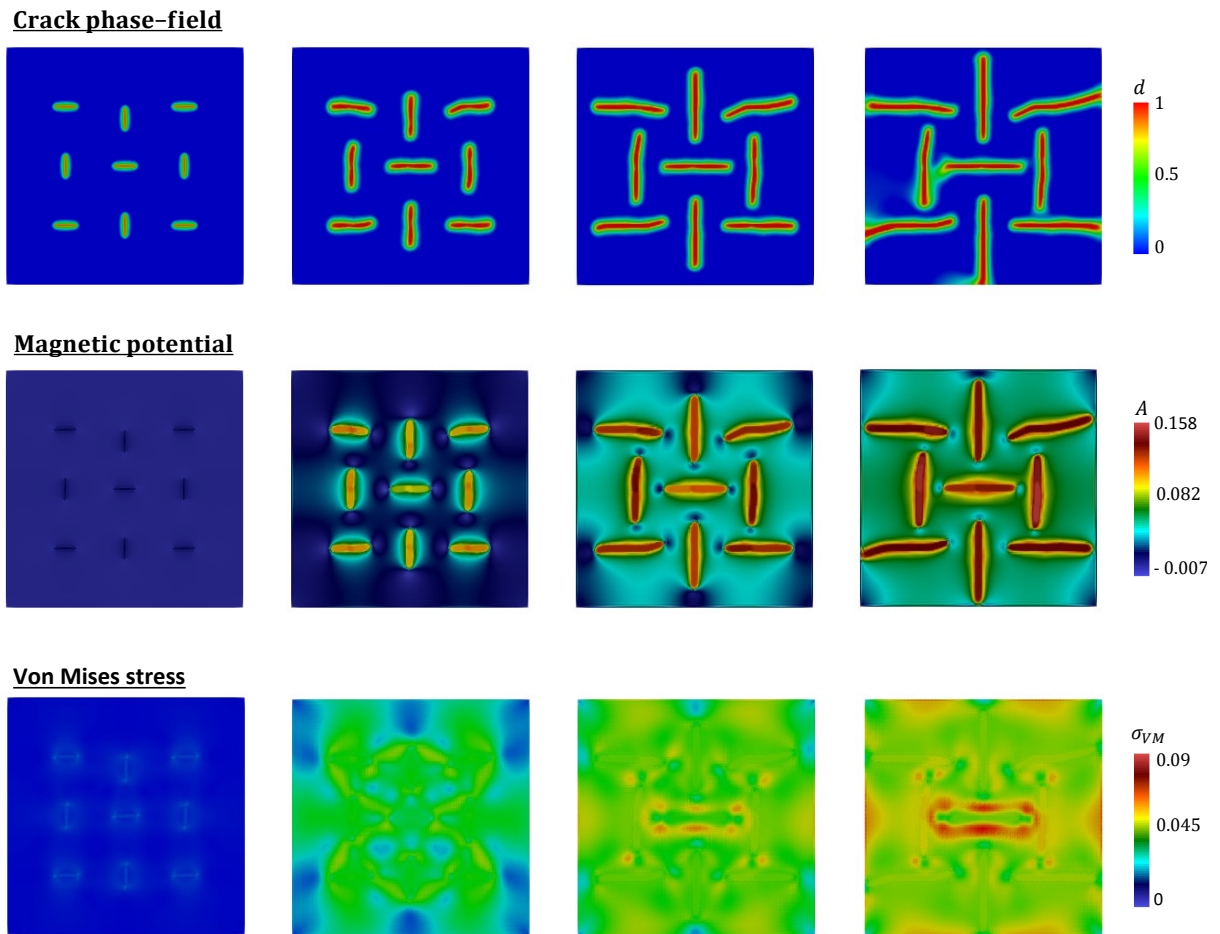


Figure 15: Example 3.2. Transversely wired plate with nine winding wires. Reference results of the magnetostrictively induced crack driven by constant electric current source induction along the predefined notches. Evolution of the crack phase-field, magnetic vector potential and von Mises stress at different time steps.

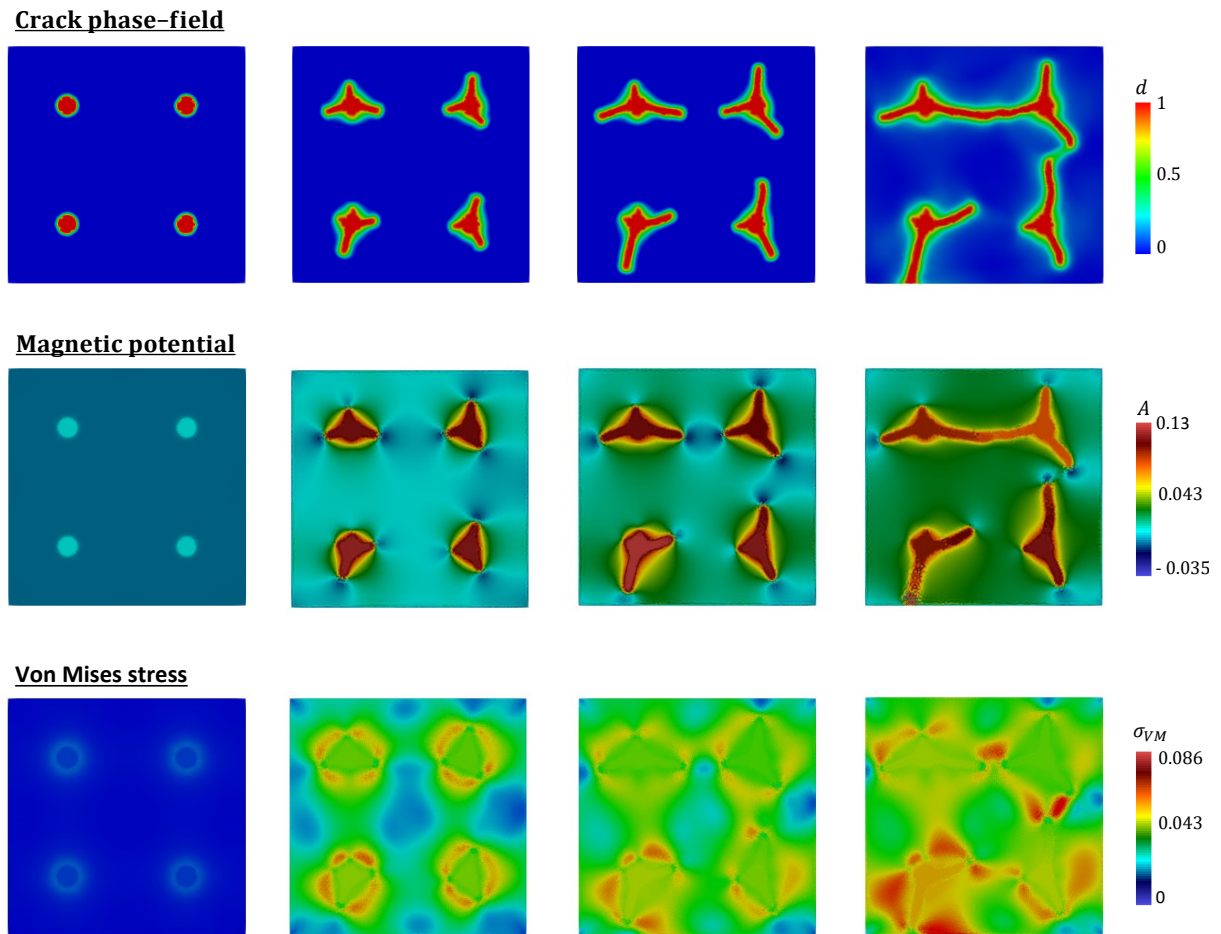


Figure 16: Example 3.3. Longitudinally wired plate with four winding wires. Reference results of the magnetostrictively induced crack driven by constant electric current source induction on the copper wires. Evolution of the crack phase-field, magnetic vector potential and von Mises stress at different time steps.

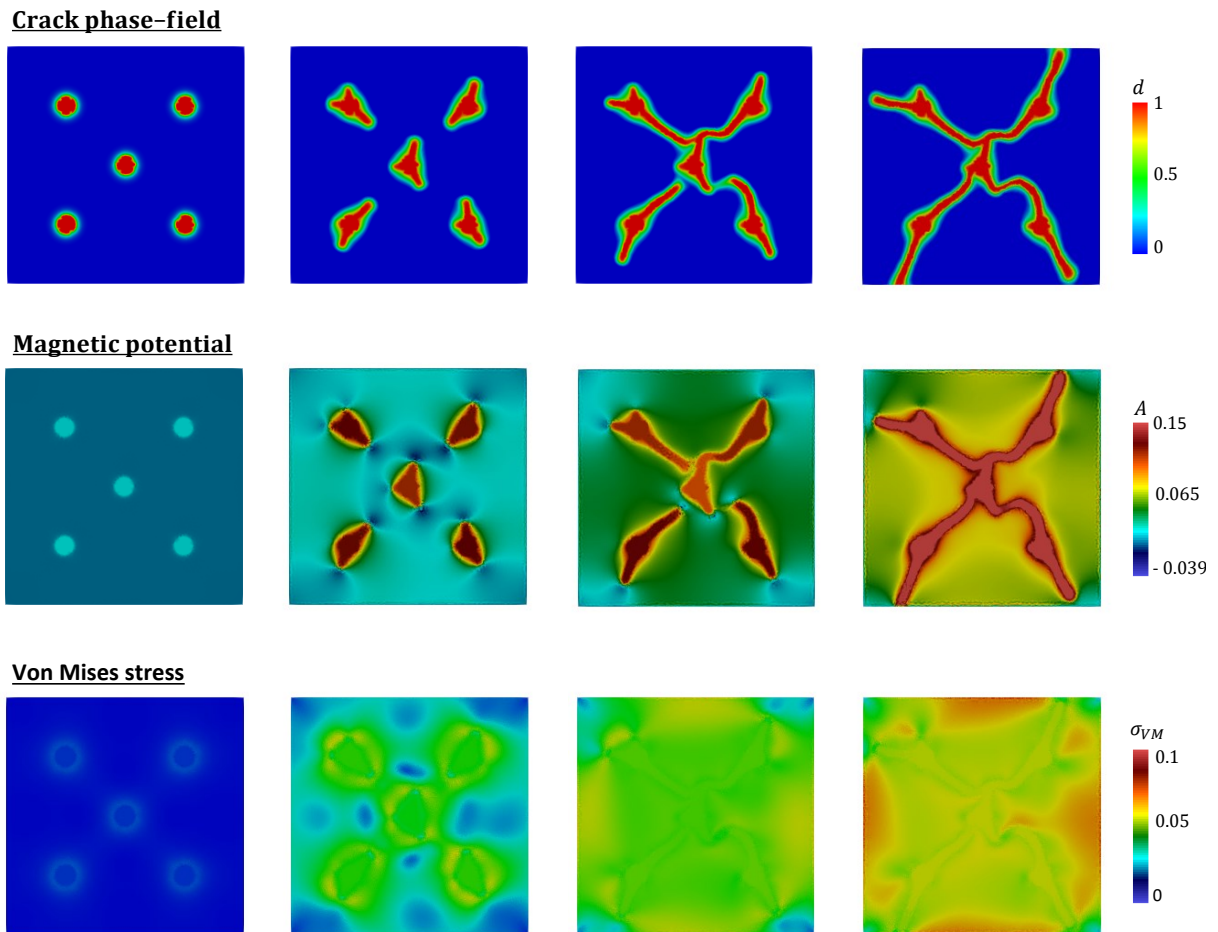


Figure 17: Example 3.4. Longitudinally wired plate with five winding wires. Reference results of the magnetostrictively induced crack driven by constant electric current source induction on the copper wires. Evolution of the crack phase-field, magnetic vector potential and von Mises stress at different time steps.

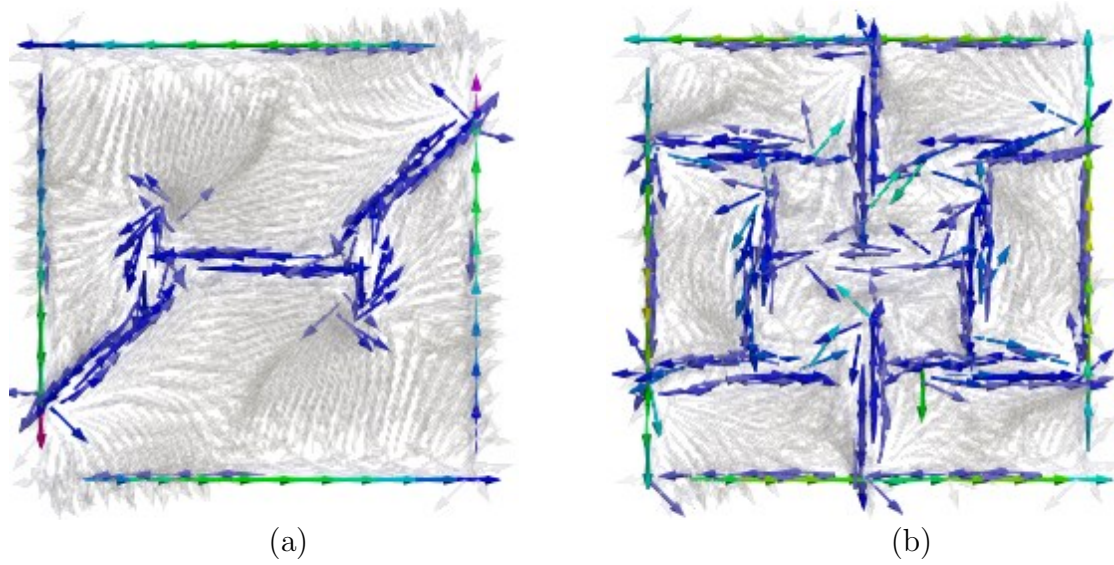


Figure 18: Transversely wired plates. The representation of magnetic field induced by the constant electric current source along the predefined notches on (a) square plate with three notches (Example 3.1), and (b) square plates with nine notches (Example 3.2).

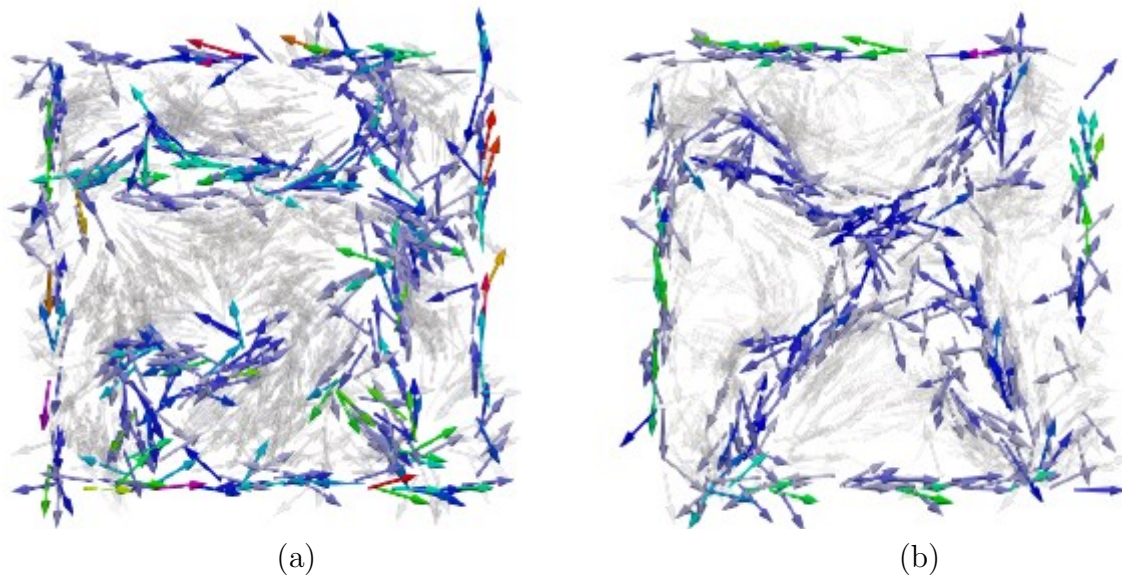


Figure 19: Longitudinally wired plates. The representation of magnetic field induced by the constant electric current source along the copper wires on square plate with (a) four copper wires (Example 3.3), and (b) five copper wires (Example 3.4).

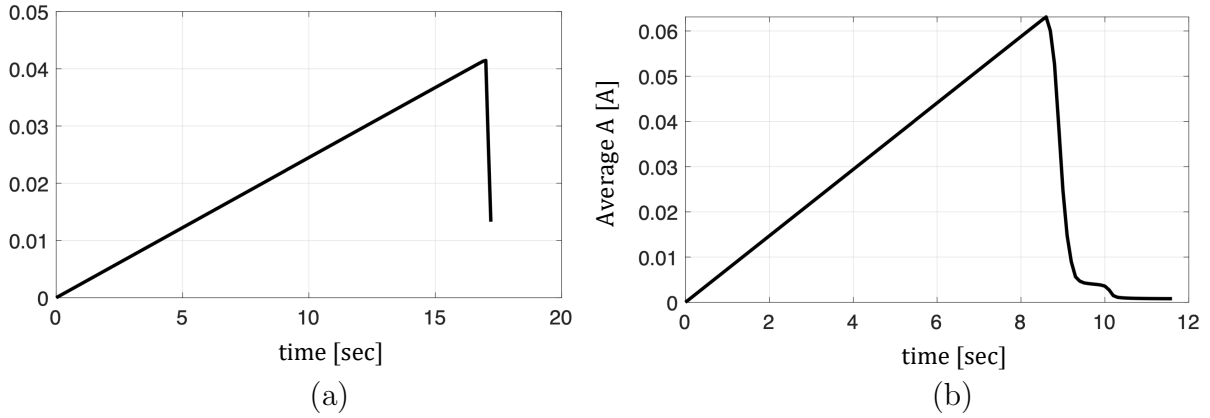


Figure 20: Longitudinally wired plates. The average value of magnetic vector potential A_{ave} over time for the square plate contains (a) three notches (Example 3.1), and (b) nine notches (Example 3.2).

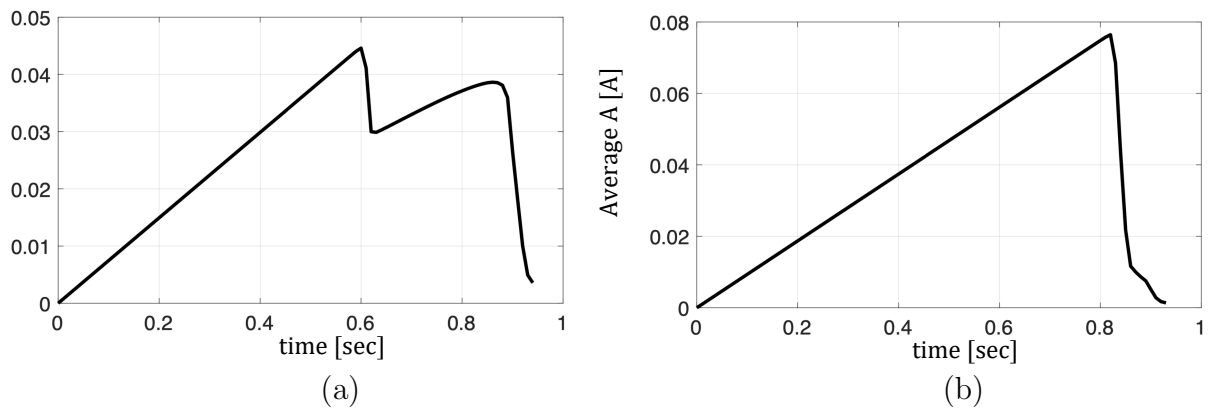


Figure 21: Transversely wired plates. The average value of magnetic vector potential A_{ave} over time for the square plate contains (a) four copper wires (Example 3.3), and (b) five copper wires (Example 3.4).

5. Conclusion

A coupled electro-magneto-mechanical model, along with the phase-field approach is developed for simulating crack growth in ferromagnetic material. The proposed coupled electro-magneto-mechanical model evaluates the evolution of the stress response and deformation of the material under the magnetostrictive effects. The magneto-mechanically-driven cracking is examined by applying the phase-field approach. To this end, we extended Maxwell's equation to a variational-based electro-magneto-elastic model, then coupled it with the phase-field approach. In this model, the total stress is additively decoupled into three parts, containing purely mechanical, purely-magnetic, and the coupled magneto-mechanical stresses. The magneto-driven deformation in a solid body is computed as a function of the magnetic field, which is implicitly defined through the magnetic vector potential.

The cracking response of the ferromagnetic material is computationally formulated on the basis of the degradation of the effective stress tensor. The degradation function is formulated as a function of the damage variable. Its initiation and propagation is developed through the thermodynamically consistent variational form of the crack phase field. The total energy functional includes the constitutive energy density functions that correspond to elastic, magnetostrictive, magnetization, and fracture contributions. In the phase-field method, the crack driving force is determined in terms of the mechanical free energy function. In the current work, the capability of the proposed model in predicting the response of the ferromagnetic material is validated by a couple of representative numerical examples. At first, we used Maxwell's equations to investigate the variation of the electric and magnetic fields in a solid body surrounded by a vacuum. Then, we extended the coupled magneto-elastic model along with the crack phase-field method to examine the cracking response under the mechanical deformation of a ferromagnetic material induced by magnetization.

Several topics for further research emerge from the present study. First, the assumption of monotonic increasing for specific current density \mathbf{J}_s could be extended to time-dependent cyclic magnetization. So, the possibility of fatigue failure in the ferromagnetic materials with magnetostrictive effects could be elaborated. For this purpose, the degradation of Griffith's energy release rate can be considered. Moreover, thermal effects, which can contribute as an additional source of failure in the ferromagnetic material, can be taken into consideration. In that case, the interaction between magnetic and thermal fields needs to be considered (e.g., in an electromagnetic rail launcher). In addition, the assumption of magnetostatics could be further relaxed (requiring the use of Nédélec elements), such that the variation of the electric displacement in time does not vanish anymore and hence causes non-zero permittivity in the electric equation.

Acknowledgment

N. Noii funded by the Priority Program DFG-SPP 2020 within its second funding phase. P. Wriggers were funded by the Deutsche Forschungsgemeinschaft (DFG, German Research Foundation) under Germany's Excellence Strategy within the Cluster of Excellence PhoenixD, EXC 2122 (project number: 390833453).

Appendix A. Approximation of the five material constants in W_{mag}

The objective is to derive the five material constants denoted as $g_i(\mathbf{x})$ in W_{mag} of (63). Recall the total form of the Helmholtz free energy function for the description of the electromagneto-mechanical response of a ferromagnetic material is introduced by

$$W(\mathbf{C}) := W_{elas}(\boldsymbol{\varepsilon}, d) + W_{mag}(\boldsymbol{\varepsilon}, \mathbf{B}; d) + W_{mos}(\boldsymbol{\varepsilon}, \mathbf{B}; d). \quad (\text{A.1})$$

and bases on five invariants

$$W(\mathbf{C}) := W_{elas}(I_1, I_2, d) + W_{mag}(I_1, I_4; d) + W_{mos}(I_5, I_6; d). \quad (\text{A.2})$$

This expression is based on invariants which express the mechanics, the magnetization and the magnetostriction of the material. The first two of these invariants describe the isotropic characteristics of the solid material as a function of the total strain tensor as follows

$$I_1(\boldsymbol{\varepsilon}) = \text{tr}(\boldsymbol{\varepsilon}) \quad \text{and} \quad I_2(\boldsymbol{\varepsilon}) = \frac{1}{2}(\boldsymbol{\varepsilon} : \boldsymbol{\varepsilon}). \quad (\text{A.3})$$

The remaining invariants I_4 , I_5 and I_6 describe the single-valued magnetization and the magnetostrictive curves as a function of the magnetic flux density \mathbf{B} . They are provided in the following expressions

$$I_4(\mathbf{B}) = \mathbf{B} \cdot \mathbf{B}, \quad I_5(\boldsymbol{\varepsilon}, \mathbf{B}) = \mathbf{B} \cdot \boldsymbol{\varepsilon} \cdot \mathbf{B} \quad \text{and} \quad I_6(\boldsymbol{\varepsilon}, \mathbf{B}) = \mathbf{B} \cdot \boldsymbol{\varepsilon}^2 \cdot \mathbf{B}. \quad (\text{A.4})$$

The Cauchy stress tensor is derived by taking the partial derivative of the total Helmholtz free energy function with respect to the total strain tensor

$$\boldsymbol{\sigma}(\boldsymbol{\varepsilon}, \mathbf{B}, d) := \frac{\partial W(\boldsymbol{\varepsilon}, \mathbf{B}, d)}{\partial \boldsymbol{\varepsilon}} = \sum_i \frac{\partial W(\boldsymbol{\varepsilon}, \mathbf{B}, d)}{\partial I_i} \frac{\partial I_i}{\partial \boldsymbol{\varepsilon}}. \quad (\text{A.5})$$

Also, the magnetization, see (65), is determined by taking the partial derivative of the total Helmholtz free energy function with respect to the magnetic flux density

$$\mathbf{M}(\boldsymbol{\varepsilon}, \mathbf{B}; d) := -\frac{\partial W(\boldsymbol{\varepsilon}, \mathbf{B}, d)}{\partial \mathbf{B}} = -\sum_i \frac{\partial W(\boldsymbol{\varepsilon}, \mathbf{B}, d)}{\partial I_i} \frac{\partial I_i}{\partial \mathbf{B}}. \quad (\text{A.6})$$

In (A.5) and (A.6), the partial derivatives of the basic invariants with respect to the strain tensor and the magnetic flux density vector are defined as

$$\begin{aligned} \frac{\partial I_1}{\boldsymbol{\varepsilon}} &= \mathbf{I} & \frac{\partial I_2}{\boldsymbol{\varepsilon}} &= \boldsymbol{\varepsilon}, & \frac{\partial I_5}{\boldsymbol{\varepsilon}} &= \boldsymbol{\varepsilon} \otimes \boldsymbol{\varepsilon}, \\ \frac{\partial I_6}{\boldsymbol{\varepsilon}} &= \mathbf{B} \otimes \mathbf{B} \cdot \boldsymbol{\varepsilon} + \boldsymbol{\varepsilon} \cdot \mathbf{B} \otimes \mathbf{B}, \\ \frac{\partial I_4}{\mathbf{B}} &= 2\mathbf{B}, & \frac{\partial I_5}{\mathbf{B}} &= \mathbf{B} \cdot \boldsymbol{\varepsilon} \quad \text{and} \quad \frac{\partial I_6}{\mathbf{B}} &= \mathbf{B} \cdot \boldsymbol{\varepsilon}^2. \end{aligned} \quad (\text{A.7})$$

Therefore, the Cauchy stress tensor in follows with

$$\begin{aligned}
 \boldsymbol{\sigma}(\boldsymbol{\varepsilon}, \mathbf{B}, d) &:= \frac{\partial W(\boldsymbol{\varepsilon}, \mathbf{B}, d)}{\partial \boldsymbol{\varepsilon}} \\
 &= g_e(d) \tilde{\boldsymbol{\sigma}}^+(\boldsymbol{\varepsilon}) + \tilde{\boldsymbol{\sigma}}^-(\boldsymbol{\varepsilon}) + \frac{1}{2} \sum_{i=0}^4 \frac{1}{i+1} \partial_{I_1} g_i \frac{I_4^{i+1}}{B_{\text{ref}}^{2i}} \mathbf{I} \\
 &\quad + \frac{g(d)}{2} \alpha_5 \mathbf{B} \otimes \mathbf{B} + \frac{g(d)}{2} \alpha_6 (\mathbf{B} \otimes \mathbf{B} \cdot \boldsymbol{\varepsilon} + \boldsymbol{\varepsilon} \cdot \mathbf{B} \otimes \mathbf{B}),
 \end{aligned} \tag{A.8}$$

see (72) and (73), as well. The constitutive equation for pure mechanics state is additively split to purely tensile contribution $\tilde{\boldsymbol{\sigma}}^+(\boldsymbol{\varepsilon})$ and purely compression contribution $\tilde{\boldsymbol{\sigma}}^-(\boldsymbol{\varepsilon})$, reads

$$\boldsymbol{\sigma}(\boldsymbol{\varepsilon}, s) := \frac{\partial W_{\text{elas}}(\boldsymbol{\varepsilon}, d)}{\partial \boldsymbol{\varepsilon}} = g_e(d) \frac{\partial \psi^+}{\partial \boldsymbol{\varepsilon}} + \frac{\partial \psi^-}{\partial \boldsymbol{\varepsilon}} = g_e(d) \tilde{\boldsymbol{\sigma}}^+ + \tilde{\boldsymbol{\sigma}}^-, \tag{A.9}$$

with

$$\tilde{\boldsymbol{\sigma}}^+(\boldsymbol{\varepsilon}) = K_n H^+(I_1) (\boldsymbol{\varepsilon} : \mathbf{I}) \mathbf{I} + 2\mu \boldsymbol{\varepsilon}^{\text{dev}}, \quad \text{and} \quad \tilde{\boldsymbol{\sigma}}^-(\boldsymbol{\varepsilon}) = K_n (1 - H^+(I_1)) (\boldsymbol{\varepsilon} : \mathbf{I}) \mathbf{I}. \tag{A.10}$$

Correspondingly magnetization vector denoted as \mathbf{M} yields:

$$\begin{aligned}
 \mathbf{M}(\boldsymbol{\varepsilon}, \mathbf{B}; d) &:= -\frac{\partial W(\boldsymbol{\varepsilon}, \mathbf{B}, d)}{\partial \mathbf{B}} \\
 &= -\sum_{i=0}^4 \frac{g_i}{i+1} \partial_{I_4} \frac{I_4^{i+1}}{B_{\text{ref}}^{2i}} - g(d) \left(\frac{1}{2} \alpha_5 \mathbf{B} \cdot \boldsymbol{\varepsilon} - \frac{1}{2} \alpha_6 \mathbf{B} \cdot \boldsymbol{\varepsilon}^2 \right),
 \end{aligned} \tag{A.11}$$

see (65), as well. Thus, the total stress tensor is derived as

$$\begin{aligned}
 \boldsymbol{\tau}(\boldsymbol{\varepsilon}, \mathbf{B}, d) &= g_e(d) \tilde{\boldsymbol{\sigma}}^+(\boldsymbol{\varepsilon}) + \tilde{\boldsymbol{\sigma}}^-(\boldsymbol{\varepsilon}) + \frac{1}{2} \sum_{i=0}^4 \frac{1}{i+1} \partial_{I_1} g_i \frac{I_4^{i+1}}{B_{\text{ref}}^{2i}} \mathbf{I} \\
 &\quad + \left(E_M \mu_0^{-1} + \sum_{i=0}^4 \frac{g_i}{i+1} \partial_{I_4} \frac{I_4^{i+1}}{B_{\text{ref}}^{2i}} + \frac{1}{2} \alpha_5 \right) \mathbf{B} \otimes \mathbf{B} \\
 &\quad - \left(\frac{E_M}{2} \mu_0^{-1} + \sum_{i=0}^4 \frac{g_i}{i+1} \partial_{I_4} \frac{I_4^{i+1}}{B_{\text{ref}}^{2i}} \right) \mathbf{B} \cdot \mathbf{B} \mathbf{I} \\
 &\quad - \left(\frac{1}{2} \alpha_5 (\mathbf{B} \cdot \boldsymbol{\varepsilon} \cdot \mathbf{B}) \mathbf{I} - \frac{1}{2} \alpha_6 (\mathbf{B} \cdot \boldsymbol{\varepsilon}^2 \cdot \mathbf{B}) \mathbf{I} \right. \\
 &\quad + \frac{1}{2} \alpha_5 \mathbf{B} \otimes \mathbf{B} \cdot \boldsymbol{\varepsilon} + \frac{1}{2} \alpha_6 \mathbf{B} \otimes \mathbf{B} \cdot \boldsymbol{\varepsilon}^2 \\
 &\quad \left. + \frac{1}{2} \alpha_6 [\mathbf{B} \otimes \mathbf{B} \cdot \boldsymbol{\varepsilon} + \boldsymbol{\varepsilon} \cdot \mathbf{B} \otimes \mathbf{B}] \right).
 \end{aligned} \tag{A.12}$$

To approximate the *homogenous response* of $g_i(I_i)$ in (A.2), we further assume (A.8) is in (i) pure magnetic loading, (ii) volume-preserving deformation and (iii) intact region

so $g(d) = 1$. As a result, we first compute the trace of the total stress tensor as follows:

$$\begin{aligned} \text{tr}(\boldsymbol{\tau}) &= 3\lambda I_1 + \frac{3}{2} \sum_{i=0}^4 \frac{1}{i+1} \frac{\partial g_i}{\partial I_1} I_4^{i+1} + 2\mu I_1 \\ &\quad - \left(\frac{1}{2\mu_0} + 2 \sum_{i=0}^4 \frac{g_i}{i+1} \frac{\partial I_4^{i+1}}{\partial I_4} - \frac{1}{2} \alpha_5 \right) I_4 - \alpha_5 I_5 + \alpha_6 I_6. \end{aligned} \quad (\text{A.13})$$

Considering the conditions of volume-preserving deformation in pure magnetic loading, we get the following relation

$$\begin{cases} \frac{3}{2} \sum_{i=0}^4 \frac{1}{i+1} \frac{\partial g_i}{\partial I_1} I_4^{i+1} - \left(\frac{1}{2\mu_0} + 2 \sum_{i=0}^4 \frac{g_i}{i+1} \frac{\partial I_4^{i+1}}{\partial I_4} - \frac{1}{2} \alpha_5 \right) I_4 = 0, \\ -\alpha_5 I_5 + \alpha_6 I_6 = 0. \end{cases} \quad (\text{A.14})$$

The functions $g_i(I_i)$ is derived from the first expression of (5) for each set of $i = \{0, 1, 2, 3, 4\}$ as follows:

$$\begin{cases} \frac{\partial g_0}{\partial I_1} = \frac{1}{3} \left(\frac{1}{\mu_0} - \alpha_5 \right) + \frac{4}{3} g_0 \\ \frac{\partial g_i}{\partial I_1} = \frac{3}{4} (i+1) g_i, \quad \text{where } i = 1, 2, 3, 4 \end{cases}, \quad (\text{A.15})$$

which finally leads to

$$\begin{cases} g_0 = \frac{3}{4} \alpha_0 \exp\left(\frac{3}{4} I_1\right) - \frac{1}{3} \left(\frac{1}{\mu_0} - \alpha_5 \right) \\ g_i = \frac{3(i+1)}{4} \alpha_i \exp\left(\frac{4(i+1)}{3} I_1\right), \quad \text{where } i=1,2,3,4. \end{cases}, \quad (\text{A.16})$$

Here, in (A.16) α_i for $i = \{0, 1, 2, 3, 4, 5\}$ refers to the material parameters depending on the ferromagnetic structure due to magnetisation effect, see [16]. Alternatively, the five material constants g_i in W_{mag} could be seen as material constants which could be calibrated in experiments.

References

- [1] S. John, J. Sirohi, G. Wang, and N. M. Wereley, "Comparison of piezoelectric, magnetostrictive, and electrostrictive hybrid hydraulic actuators," *Journal of intelligent material systems and structures*, vol. 18, no. 10, pp. 1035–1048, 2007.
- [2] Y. Bar-Cohen and Q. Zhang, "Electroactive polymer actuators and sensors," *MRS bulletin*, vol. 33, no. 3, pp. 173–181, 2008.
- [3] K. J. Kim and S. Tadokoro, "Electroactive polymers for robotic applications," *Artificial Muscles and Sensors*, vol. 23, p. 291, 2007.

-
- [4] D. Berlincourt, *Ultrasonic transducer materials*. Springer, 1971.
- [5] R. Guldiken and O. Onen, “5 - mems ultrasonic transducers for biomedical applications,” in *MEMS for Biomedical Applications* (S. Bhansali and A. Vasudev, eds.), Woodhead Publishing Series in Biomaterials, pp. 120–149, Woodhead Publishing, 2012.
- [6] D. Damjanovic and R. Newnham, “Electrostrictive and piezoelectric materials for actuator applications,” *Journal of intelligent material systems and structures*, vol. 3, no. 2, pp. 190–208, 1992.
- [7] B. C. Sekhar, B. Dhanalakshmi, B. S. Rao, S. Ramesh, K. V. Prasad, P. S. Rao, and B. P. Rao, “Piezoelectricity and its applications,” *Multifunctional Ferroelectric Materials*, p. 71, 2021.
- [8] J. P. Joule, “On a new class of magnetic forces,” *Ann. Electr. Magn. Chem*, vol. 8, no. 1842, pp. 219–224, 1842.
- [9] E. Villari, “Intorno alle modificazioni del momento magnetico di una verga di ferro e di acciaio, prodotte per la trazione della medesima e pel passaggio di una corrente attraverso la stessa,” *Il Nuovo Cimento (1855-1868)*, vol. 20, no. 1, pp. 317–362, 1864.
- [10] C. Birk, M. Reichel, and J. Schröder, “Magnetostatic simulations with consideration of exterior domains using the scaled boundary finite element method,” *Computer Methods in Applied Mechanics and Engineering*, vol. 399, p. 115362, 2022.
- [11] I. Brigadnov and A. Dorfmann, “Mathematical modeling of magneto-sensitive elastomers,” *International Journal of Solids and Structures*, vol. 40, no. 18, pp. 4659–4674, 2003.
- [12] A. Dorfmann and R. Ogden, “Magnetoelastic modelling of elastomers,” *European Journal of Mechanics - A/Solids*, vol. 22, no. 4, pp. 497–507, 2003.
- [13] A. Dorfmann, R. Ogden, and G. Saccomandi, “Universal relations for non-linear magnetoelastic solids,” *International Journal of Non-Linear Mechanics*, vol. 39, no. 10, pp. 1699–1708, 2004.
- [14] J. D. Thomas and N. Triantafyllidis, “On electromagnetic forming processes in finitely strained solids: Theory and examples,” *Journal of the Mechanics and Physics of Solids*, vol. 57, no. 8, pp. 1391–1416, 2009.
- [15] A. Belahcen, K. Fonteyn, S. Fortino, and R. Kouhia, “A coupled magnetoelastic model for ferromagnetic materials,” *Proc. of the IX Finnish Mechanics Days. von Herten R., Halme T.(eds.)*, pp. 673–682, 2006.
- [16] K. A. Fonteyn, *Energy-based magneto-mechanical model for electrical steel sheets*. PhD thesis, Aalto-yliopiston Teknillinen Korkeakoulu, 2010.
- [17] K. Fonteyn, A. Belahcen, R. Kouhia, P. Rasilo, and A. Arkkio, “Fem for directly coupled magneto-mechanical phenomena in electrical machines,” *IEEE Transactions on Magnetics*, vol. 46, no. 8, pp. 2923–2926, 2010.
- [18] P. Rasilo, D. Singh, J. Jeronen, U. Aydin, F. Martin, A. Belahcen, L. Daniel, and R. Kouhia, “Flexible identification procedure for thermodynamic constitutive models for magnetostrictive materials,” *Proceedings of the Royal Society A*, vol. 475, no. 2223, p. 20180280, 2019.
- [19] C. Miehe, D. Rosato, and B. Kiefer, “Variational principles in dissipative electromagneto-mechanics: a framework for the macro-modeling of functional materials,” *International Journal for Numerical Methods in Engineering*, vol. 86, no. 10, pp. 1225–1276, 2011.

-
- [20] C. Miehe and G. Ethiraj, “A geometrically consistent incremental variational formulation for phase field models in micromagnetics,” *Computer methods in applied mechanics and engineering*, vol. 245, pp. 331–347, 2012.
- [21] G. Ethiraj, *Computational modeling of ferromagnetics and magnetorheological elastomers*. 2014.
- [22] G. Ethiraj and C. Miehe, “Multiplicative magneto-elasticity of magnetosensitive polymers incorporating micromechanically-based network kernels,” *International Journal of Engineering Science*, vol. 102, pp. 93–119, 2016.
- [23] N. Hanappier, E. Charkaluk, and N. Triantafyllidis, “A coupled electromagnetic-thermomechanical approach for the modeling of electric motors,” *Journal of the Mechanics and Physics of Solids*, vol. 149, p. 104315, 2021.
- [24] B. Zhang, Y. Kou, K. Jin, and X. Zheng, “A multi-field coupling model for the magnetic-thermal-structural analysis in the electromagnetic rail launch,” *Journal of Magnetism and Magnetic Materials*, vol. 519, p. 167495, 2021.
- [25] Z. Ma, H. Zhao, W. Liu, and L. Ren, “Thermo-mechanical coupled in situ fatigue device driven by piezoelectric actuator,” *Precision Engineering*, vol. 46, pp. 349–359, 2016.
- [26] L. Zhou, J. Tang, W. Tian, B. Xue, and X. Li, “A multi-physics coupling cell-based smoothed finite element micromechanical model for the transient response of magneto-electro-elastic structures with the asymptotic homogenization method,” *Thin-Walled Structures*, vol. 165, p. 107991, 2021.
- [27] G. A. Francfort and J.-J. Marigo, “Revisiting brittle fracture as an energy minimization problem,” *Journal of the Mechanics and Physics of Solids*, vol. 46, no. 8, pp. 1319–1342, 1998.
- [28] B. Bourdin, G. A. Francfort, and J.-J. Marigo, “The variational approach to fracture,” *Journal of Elasticity*, vol. 91, no. 1, pp. 5–148, 2008.
- [29] G. Dal Maso and R. Toader, “A model for the quasi-static growth of brittle fractures: Existence and approximation results,” *Archive for Rational Mechanics and Analysis*, vol. 162, no. 2, pp. 101–135, 2002.
- [30] D. B. Mumford and J. Shah, “Optimal approximations by piecewise smooth functions and associated variational problems,” *Communications on Pure and Applied Mathematics*, 1989.
- [31] V. Hakim and A. Karma, “Laws of crack motion and phase-field models of fracture,” *Journal of the Mechanics and Physics of Solids*, vol. 57, no. 2, pp. 342–368, 2009.
- [32] C. Miehe, M. Hofacker, and F. Welschinger, “A phase field model for rate-independent crack propagation: Robust algorithmic implementation based on operator splits,” *Computer Methods in Applied Mechanics and Engineering*, vol. 199, no. 45, pp. 2765–2778, 2010.
- [33] C. Miehe, F. Welschinger, and M. Hofacker, “A phase field model of electromechanical fracture,” *Journal of the Mechanics and Physics of Solids*, vol. 58, no. 10, pp. 1716–1740, 2010.
- [34] C. Linder and C. Miehe, “Effect of electric displacement saturation on the hysteretic behavior of ferroelectric ceramics and the initiation and propagation of cracks in piezoelectric ceramics,” *Journal of the Mechanics and Physics of Solids*, vol. 60, no. 5, pp. 882–903, 2012.
- [35] P. Monk *et al.*, *Finite element methods for Maxwell’s equations*. Oxford University Press, 2003.

-
- [36] P. W. Gross, P. W. Gross, P. R. Kotiuga, and R. P. Kotiuga, *Electromagnetic theory and computation: a topological approach*, vol. 48. Cambridge University Press, 2004.
- [37] N. Noii, M. Fan, T. Wick, and Y. Jin, “A quasi-monolithic phase-field description for orthotropic anisotropic fracture with adaptive mesh refinement and primal–dual active set method,” *Engineering Fracture Mechanics*, vol. 258, p. 108060, 2021.
- [38] N. Noii, F. Aldakheel, T. Wick, and P. Wriggers, “An adaptive global–local approach for phase-field modeling of anisotropic brittle fracture,” *Computer Methods in Applied Mechanics and Engineering*, vol. 361, p. 112744, 2020.
- [39] J. Shipman, J. D. Wilson, and C. A. Higgins, *An introduction to physical science*. Cengage Learning, 2012.
- [40] W. Emery and A. Camps, “Chapter 2 - basic electromagnetic concepts and applications to optical sensors,” in *Introduction to Satellite Remote Sensing* (W. Emery and A. Camps, eds.), pp. 43–83, Elsevier, 2017.
- [41] N. A. Spaldin, *Magnetic materials: fundamentals and applications*. Cambridge university press, 2010.
- [42] J. Fliegans, O. Tosoni, N. Dempsey, and G. Delette, “Modeling of demagnetization processes in permanent magnets measured in closed-circuit geometry,” *Applied Physics Letters*, vol. 116, no. 6, p. 062405, 2020.
- [43] C. Bruzzese, *Theory of Electrical Machines*. Società Editrice Esculapio, 2022.
- [44] J. D. Jackson, “Classical electrodynamics,” 1999.
- [45] F. Melia, *Electrodynamics*. Chicago Lectures in Physics, University of Chicago Press, 2001.
- [46] H. van Hees, “Comment on ‘defining the electromagnetic potentials’,” *European Journal of Physics*, vol. 42, no. 2, p. 028003, 2021.
- [47] T. Maudlin, “Ontological clarity via canonical presentation: Electromagnetism and the aharonov–bohm effect,” *Entropy*, vol. 20, no. 6, p. 465, 2018.
- [48] J. D. Powell and A. E. Zielinski, “Two-dimensional current diffusion in the rails of a railgun,” tech. rep., Army Research LAB ABERDEEN Proving Ground MD Weapons and Materials Research, 2008.
- [49] B. Zhang, Y. Kou, K. Jin, and X. Zheng, “A multi-field coupling model for the magnetic-thermal-structural analysis in the electromagnetic rail launch,” *Journal of Magnetism and Magnetic Materials*, vol. 519, p. 167495, 2021.
- [50] B. Bourdin, G. Francfort, and J.-J. Marigo, “Numerical experiments in revisited brittle fracture,” *Journal of the Mechanics and Physics of Solids*, vol. 48, no. 4, pp. 797–826, 2000.
- [51] G. Francfort and J.-J. Marigo, “Revisiting brittle fracture as an energy minimization problem,” *Journal of the Mechanics and Physics of Solids*, vol. 46, no. 8, pp. 1319–1342, 1998.
- [52] D. Kienle, F. Aldakheel, and M.-A. Keip, “A finite-strain phase-field approach to ductile failure of frictional materials,” *International Journal of Solids and Structures*, vol. 172, pp. 147–162, 2019.
- [53] M. Dittmann, F. Aldakheel, J. Schulte, F. Schmidt, M. Krüger, P. Wriggers, and C. Hesch, “Phase-field modeling of porous-ductile fracture in non-linear thermo-elasto-plastic solids,” *Computer Methods in Applied Mechanics and Engineering*, vol. 361, p. 112730, 2020.

-
- [54] H. Ruan, S. Rezaei, Y. Yang, D. Gross, and B.-X. Xu, “A thermo-mechanical phase-field fracture model: Application to hot cracking simulations in additive manufacturing,” *Journal of the Mechanics and Physics of Solids*, p. 105169, 2022.
- [55] Z. Peng, Q. Wang, W. Zhou, X. Chang, Q. Yue, and C. Huang, “Meso-scale simulation of thermal fracture in concrete based on the coupled thermal–mechanical phase-field model,” *Construction and Building Materials*, vol. 403, p. 133095, 2023.
- [56] M. Ambati, R. Kruse, and L. De Lorenzis, “A phase-field model for ductile fracture at finite strains and its experimental verification,” *Computational Mechanics*, vol. 57, pp. 149–167, 2016.
- [57] B. Yin and M. Kaliske, “A ductile phase-field model based on degrading the fracture toughness: Theory and implementation at small strain,” *Computer Methods in Applied Mechanics and Engineering*, vol. 366, p. 113068, 2020.
- [58] N. Noii, A. Khodadadian, J. Ulloa, F. Aldakheel, T. Wick, S. François, and P. Wriggers, “Bayesian inversion for unified ductile phase-field fracture,” *Computational Mechanics*, vol. 68, no. 4, pp. 943–980, 2021.
- [59] Y. Heider and W. Sun, “A phase field framework for capillary-induced fracture in unsaturated porous media: Drying-induced vs. hydraulic cracking,” *Computer Methods in Applied Mechanics and Engineering*, vol. 359, p. 112647, 2020.
- [60] J. Ulloa, N. Noii, R. Alessi, F. Aldakheel, G. Degrande, and S. François, “Variational modeling of hydromechanical fracture in saturated porous media: A micromechanics-based phase-field approach,” *Computer Methods in Applied Mechanics and Engineering*, vol. 396, p. 115084, 2022.
- [61] N. Noii and T. Wick, “A phase-field description for pressurized and non-isothermal propagating fractures,” *Computer Methods in Applied Mechanics and Engineering*, vol. 351, pp. 860–890, 2019.
- [62] N. Noii, A. Khodadadian, J. Ulloa, F. Aldakheel, T. Wick, S. François, and P. Wriggers, “Bayesian inversion with open-source codes for various one-dimensional model problems in computational mechanics,” *Archives of Computational Methods in Engineering*, pp. 1–34, 2022.
- [63] N. Noii, A. Khodadadian, and F. Aldakheel, “Probabilistic failure mechanisms via monte carlo simulations of complex microstructures,” *Computer Methods in Applied Mechanics and Engineering*, vol. 399, p. 115358, 2022.
- [64] N. Noii, A. Khodadadian, and T. Wick, “Bayesian inversion for anisotropic hydraulic phase-field fracture,” *Computer Methods in Applied Mechanics and Engineering*, vol. 386, p. 114118, 2021.
- [65] N. Noii, A. Khodadadian, and T. Wick, “Bayesian inversion using global-local forward models applied to fracture propagation in porous media,” *International Journal for Multiscale Computational Engineering*, vol. 20, no. 3, 2022.
- [66] N. Noii, H. A. Jahangiry, and H. Waisman, “Level-set topology optimization for ductile and brittle fracture resistance using the phase-field method,” *Computer Methods in Applied Mechanics and Engineering*, vol. 409, p. 115963, 2023.
- [67] Z. Liu, J. Reinoso, and M. Paggi, “Phase field modeling of brittle fracture in large-deformation solid shells with the efficient quasi-newton solution and global–local approach,” *Computer Methods in Applied Mechanics and Engineering*, vol. 399, p. 115410, 2022.
- [68] F. Aldakheel, N. Noii, T. Wick, and P. Wriggers, “A global–local approach for hydraulic phase-field fracture in poroelastic media,” *Computers and Mathematics with Applications*, 2020.

-
- [69] F. Aldakheel, N. Noii, T. Wick, O. Allix, and P. Wriggers, “Multilevel global–local techniques for adaptive ductile phase-field fracture,” *Computer Methods in Applied Mechanics and Engineering*, vol. 387, p. 114175, 2021.
- [70] T. Hageman and E. Martínez-Pañeda, “An electro-chemo-mechanical framework for predicting hydrogen uptake in metals due to aqueous electrolytes,” *Corrosion Science*, vol. 208, p. 110681, 2022.
- [71] J.-Y. Wu and Y.-F. Hong, “Crack nucleation and propagation of electromagneto-thermo-mechanical fracture in bulk superconductors during magnetization,” *Journal of the Mechanics and Physics of Solids*, p. 105168, 2022.
- [72] Y. Zhao, R. Wang, and E. Martínez-Pañeda, “A phase field electro-chemo-mechanical formulation for predicting void evolution at the li–electrolyte interface in all-solid-state batteries,” *Journal of the Mechanics and Physics of Solids*, vol. 167, p. 104999, 2022.
- [73] C. Kuhn, A. Schlüter, and R. Müller, “On degradation functions in phase field fracture models,” *Computational Materials Science*, vol. 108, pp. 374–384, 2015.
- [74] J.-Y. Wu, “A unified phase-field theory for the mechanics of damage and quasi-brittle failure,” *Journal of the Mechanics and Physics of Solids*, vol. 103, pp. 72–99, 2017.
- [75] J.-Y. Wu, V. Nguyen, C. Nguyen, D. Sutula, S. Bordas, and S. Sinaie, “Phase field modeling of fracture,” *Advances in Applied Mechancis: Multi-Scale Theory and Computation*, vol. 52, 2018.
- [76] C. Miehe, M. Hofacker, and F. Welschinger, “A phase field model for rate-independent crack propagation: Robust algorithmic implementation based on operator splits,” *Computer Methods in Applied Mechanics and Engineering*, vol. 199, no. 45-48, pp. 2765–2778, 2010.
- [77] C. Miehe, L.-M. Schaezel, and H. Ulmer, “Phase field modeling of fracture in multi-physics problems. part i. balance of crack surface and failure criteria for brittle crack propagation in thermo-elastic solids,” *Computer Methods in Applied Mechanics and Engineering*, vol. 294, pp. 449–485, 2015.
- [78] S. Lee, M. F. Wheeler, and T. Wick, “Pressure and fluid-driven fracture propagation in porous media using an adaptive finite element phase field model,” *Computer Methods in Applied Mechanics and Engineering*, vol. 305, pp. 111–132, 2016.
- [79] C. Miehe and S. Mauthe, “Phase field modeling of fracture in multi-physics problems. part iii. crack driving forces in hydro-poro-elasticity and hydraulic fracturing of fluid-saturated porous media,” *Computer Methods in Applied Mechanics and Engineering*, vol. 304, pp. 619–655, 2016.
- [80] Y.-H. Pao and K. Hutter, “Electrodynamics for moving elastic solids and viscous fluids,” *Proceedings of the IEEE*, vol. 63, no. 7, pp. 1011–1021, 1975.
- [81] L. Daniel, L. Bernard, and O. Hubert, “Multiscale modeling of magnetic materials,” 2020.
- [82] A. Flatau, M. Dapino, and F. Calkins, “5.26 - magnetostrictive composites,” in *Comprehensive Composite Materials* (A. Kelly and C. Zweben, eds.), pp. 563–574, Oxford: Pergamon, 2000.
- [83] C. Gao, Z. Zeng, S. Peng, and C. Shuai, “Magnetostrictive alloys: Promising materials for biomedical applications,” *Bioactive Materials*, vol. 8, pp. 177–195, 2022.
- [84] M. J. Dapino, “On magnetostrictive materials and their use in adaptive structures,” *Structural Engineering and Mechanics*, vol. 17, no. 3-4, pp. 303–330, 2004.

-
- [85] A. Khodadadian, N. Noii, M. Parvizi, M. Abbaszadeh, T. Wick, and C. Heitzinger, “A bayesian estimation method for variational phase-field fracture problems,” *Computational Mechanics*, vol. 66, no. 4, pp. 827–849, 2020.
- [86] Q. Wang, Y. Feng, W. Zhou, Y. Cheng, and G. Ma, “A phase-field model for mixed-mode fracture based on a unified tensile fracture criterion,” *Computer Methods in Applied Mechanics and Engineering*, vol. 370, p. 113270, 2020.
- [87] Q. Wang, Q. Yue, W. Zhou, Y. Feng, and X. Chang, “Modeling of both tensional-shear and compressive-shear fractures by a unified phase-field model,” *Applied Mathematical Modelling*, vol. 117, pp. 162–196, 2023.
- [88] A. Kovetz, *Electromagnetic theory*, vol. 975. Oxford University Press Oxford, 2000.
- [89] B. Wu and M. Destrade, “Wrinkling of soft magneto-active plates,” *International Journal of Solids and Structures*, vol. 208, pp. 13–30, 2021.
- [90] C. Trimarco, “Stresses and momenta in electromagnetic materials,” *Mechanics Research Communications*, vol. 29, no. 6, pp. 485–492, 2002.
- [91] X. Zheng and K. Jin, “Magnetic force models for magnetizable elastic bodies in the magnetic field,” *From Waves in Complex Systems to Dynamics of Generalized Continua: Tributes to Professor Yih-Hsing Pao on His 80th Birthday*, pp. 353–383, 2011.
- [92] K. Henjes, “The traction force in magnetic separators,” *Measurement Science and Technology*, vol. 5, no. 9, p. 1105, 1994.
- [93] C. Rinaldi and H. Brenner, “Body versus surface forces in continuum mechanics: Is the maxwell stress tensor a physically objective cauchy stress?,” *Physical Review E*, vol. 65, no. 3, p. 036615, 2002.
- [94] S. A. Mauthe, *Variational multiphysics modeling of diffusion in elastic solids and hydraulic fracturing in porous media*. Stuttgart: Institut für Mechanik (Bauwesen), 2017.
- [95] C. Miehe, S. Mauthe, and S. Teichtmeister, “Minimization principles for the coupled problem of darcy–biot-type fluid transport in porous media linked to phase field modeling of fracture,” *Journal of the Mechanics and Physics of Solids*, vol. 82, pp. 186–217, 2015.
- [96] J. Li and Y.-T. Chen, *Computational partial differential equations using MATLAB®*. Crc Press, 2019.
- [97] E. Garcia, *Solution to the instationary Maxwell equations with charges in non-convex domains*. PhD thesis, PhD thesis, Université Paris VI, France, 2002.
- [98] E. Jamelot, “Solution to maxwell equations with continuous galerkin finite elements,” *Ph. D. Thesis, Ecole Polytechnique, Palaiseau, France*, 2005.
- [99] P. Ciarlet and E. Jamelot, “Continuous galerkin methods for solving the time-dependent maxwell equations in 3d geometries,” *Journal of Computational Physics*, vol. 226, no. 1, pp. 1122–1135, 2007.
- [100] M. Asadzadeh and L. Beilina, “A stabilized p1 domain decomposition finite element method for time harmonic maxwell’s equations,” *Mathematics and Computers in Simulation*, vol. 204, pp. 556–574, 2023.
- [101] G. Meunier, “The finite element method for electromagnetic modeling,” 2010.
- [102] J. R. Cardoso, *Electromagnetics through the finite element method: A simplified approach using Maxwell’s equations*. Crc Press, 2016.

-
- [103] J. P. A. Bastos and N. Sadowski, *Electromagnetic modeling by finite element methods*. CRC press, 2003.
- [104] M. Alnæs, J. Blechta, J. Hake, A. Johansson, B. Kehlet, A. Logg, C. Richardson, J. Ring, M. E. Rognes, and G. N. Wells, “The fenics project version 1.5,” *Archive of Numerical Software*, vol. 3, no. 100, 2015.
- [105] G. N. W. e. a. A. Logg, K.-A. Mardal, *Automated Solution of Differential Equations by the Finite Element Method*. Springer, 2012.
- [106] Q. Yue, Q. Wang, W. Zhou, T. Rabczuk, X. Zhuang, B. Liu, and X. Chang, “An efficient adaptive length scale insensitive phase-field model for three-dimensional fracture of solids using trilinear multi-node elements,” *International Journal of Mechanical Sciences*, vol. 253, p. 108351, 2023.